Department of Physics and Astronomy

University of Heidelberg

Master thesis

in Physics

submitted by

Julia Jäger

born in Karlsruhe (Germany)

2021

Improved 3D-imaging detection at the Cryogenic Storage Ring

This Master thesis has been carried out by Julia Jäger

at the

Max Planck Institute for Nuclear Physics

under the supervision of

Prof. Dr. Andreas Wolf

Dr. Oldřich Novotný

Verbesserte 3D-Bildgebung am Kryogenen Speichering CSR:

Die Untersuchung elektroneninduzierter molekularer Fragmentierungsprozesse in Fast-Beam-Experimenten stellt hohe Anforderungen an die technische Realisierung geeigneter Detektionsverfahren. Eine vollständige Rekonstruktion der gesamten freigesetzen kinetischen Energie und damit detaillierte Informationen über die zugrundeliegenden physikalischen Prozesse können nur aus der vollständig korrelierten Messung von Abständen abgeleitet werden. Daher muss der Detektor beim Nachweisen der Reaktionsprodukte in der Lage sein, sowohl die Positionen auf der Detektoroberfläche als auch die zeitlichen Differenzen zwischen dem Auftreffen verschiedener Fragmente mit sehr hoher Auflösung zu messen. In dieser Arbeit wurde erstmals eine neue Zeitauslese für den 3D-Imaging-Detektor NICE am kryogenen Speicherring CSR in Heidelberg aufgebaut und getestet. Die Verbesserung basiert auf der Silizium-Photomultiplier-Technik, bestehend aus einem Mehrpixeldetektor mit hoher intrinsischer Zeitauflösung. Erste Leistungstests zeigen vielversprechende Ergebnisse: Es war möglich, räumlich gut getrennte Einschläge mit einer Zeitdifferenz von bis zu Null aufzulösen, was die Zeitauflösungsgrenze des vorherigen Aufbaus übertrifft.

Improved 3D-Imaging Detection at the Cryogenic Storage Ring:

The study of electron induced molecular fragmentation processes in fast-beam experiments sets high demands on the technical realization of appropriate detection techniques. A complete reconstruction of the total kinetic energy release and thus detailed physical information of this process can only be deduced from the fully correlated measurement of distances. Therefore, the reaction product detector must be able to measure both the impact positions on the detectors surface as well as the time difference between impacts with the highest resolution. In this work a new timing readout for the 3D-imaging detector NICE at the Cryogenic Storage Ring in Heidelberg was set up and tested for the first time. The upgrade is based on the silicon photomultiplier technology, employing a multi-pixel detector with high intrinsic time resolution. First performance test show promising results: it was possible to resolve spatially well separated impacts with a time difference down to zero, exceeding the time resolution limit of the pre-existing setup.

Contents

1 Introduction

Gas-phase reactions of molecules play an important role for chemical and physical changes of matter in many environments, including low density plasmas [1], the earth's atmosphere [2] or the interstellar space [3]. Several production and destruction processes regulate the abundance of the different components.

Among various neutralization processes, an important pathway for positively charged molecular ions, e.g., in interstellar clouds, is *dissociative recombination* (DR) [4]. When an electron is in the vicinity of a molecular ion they can recombine, leading to the separation of the molecule into its atomic fragments. DR can be described in the following way: Let's consider a diatomic molecular ion AB^+ in an initial vibrational v^+ and rotational state J^+, which collides with an electron of energy E. This results in the electron being captured and forming an excited neutral molecule. The exoergic nature of the reaction then leads to dissociation in two neutral fragments A and B. The energy excess goes partly into internal excitation of the fragments and partly into kinetic energy release E_{KER}:

$$AB^+(v^+, J^+) + \mathrm{e}^-(E) \rightarrow A(n, l) + B(n', l') + E_{KER}, \tag{1.1}$$

where A and B are characterized by their principal n (n') and orbital angular l (l') momentum quantum numbers.

The capture of the electron promotes the system onto a repulsive electronic state either directly [5] or over an intermediate bound Rydberg state (indirect DR) [6], leading to fragmentation at sufficiently large internuclear distance. Thus, the expanding fragments carry the information on the reaction pathway and consequently they provide access to the fundamental fragmentation mechanism.

Investigating the kinetic energy distributed among the fragments gives insight in the fragmentation process as the final product states can be derived using the energy balance [7]. For a deeper understanding of the undergone reaction, the electronic symmetry can be derived by investigating the dependence of the reaction cross section on the orientation of the molecule with respect to the collision vector [8].

To study the mechanisms driving dissociative recombination, it is important to bring electrons and ions together at well defined energies. An excellent tool for this are storage rings employing an electron cooler section, where electron and ion beams can be aligned at relative energies down to the meV-range [9, 10, 11]. Compared to the fast ion beam (reaching energies up to 300 keV), the relative kinetic energy of the neutral DR reaction products is small (in the eV range) resulting in the effect, that the trajectories of all neutral fragments are concentrated in forward direction in a narrow cone. This greatly simplifies collection of the reaction products on a relatively small detector area, allowing to detect all reaction products, thus obtaining a full kinematic picture of the undergone reaction.

The final kinetic energy release in the dissociation process and the angle of the molecular axis with respect to the beam is derived from the fully correlated measurement of the fragments distances. Using *3D-imaging* detection techniques, this information can be inferred from measuring the position of the impinging particles in the detector plane and their relative impact times.

The simultaneous measurement of impact position and timing information resolution in the ns domain needs complex detection techniques. The 3D-imaging detector for neutral fragments NICE [12], implemented at the Cryogenic Storage Ring in Heidelberg, combines a microchannel plate with a non-segmented phosphor screen anode, allowing for position measurements with a high-speed CMOS camera and time measurements using the electrical signal induced on the phosphor screen anode with a possible precision of ~ 1 ns. Due to the finite width of the induced pulses, the impacts cannot be resolved for time differences shorter than ~ 15 ns. This limited time resolution results in a loss of information for DR reaction products impinging close together in time.

To improve the time resolution of the NICE detector, a dedicated timing readout with independent segments is needed to distinguish signals close in time. Within the present work, the NICE detector was upgraded with a silicon photomultiplier array with multiple pixels and good intrinsic time resolution, allowing for a time resolution down to 0 ns if independent pixels are hit.

Outline of this work

The introduction and motivation of this work is followed by a brief description of the Cryogenic Storage Ring (CSR) and the NICE detector including a presentation of applied imaging technique in Chapter 2.

Chapter 3 starts with a general introduction to silicon photomultipliers continuing with the implementation in the existing detection setup and the synchronization of two involved data acquisition systems.

The SiPM setup was tested during the OH^+ beamtime at the CSR in February 2021. The experimental results are presented and discussed in Chapter 4. Hereby the primary focus is on the imaging and timing performance of the SiPM setup.

The concluding Chapter 5 summarizes the key achievements and results and gives an outlook for future improvements.

2 Experimental setup

This chapter first gives a brief overview of the cryogenic storage ring (CSR) and then focuses on recombination measurements using a merged-beam setup, including the recombination product detection. For this purpose, the principle of neutral-fragment imaging and the setup and operating principle of the NICE detector are discussed in more detail.

2.1 The Cryogenic Storage Ring

The cryogenic storage ring CSR at the Max Planck Institute for Nuclear Physics in Heidelberg is a unique tool to study low energy reactions of atoms, molecules and clusters [9]. Its electrostatic nature enables mass independent ion storage at kinetic energies from 20 keV to 300 keV and its cryogenic nature allows the storage of these keV ion beams with low beam losses due to suppressed residual gas scattering. The CSR is capable of supporting temperatures down to 2 K, which is made possible by the layered structure of the ring. The inner experimental beam tube is at its center, with ultra-high vacuum levels reaching down to 10^{-14} mbar. It is surrounded by the isolation vacuum chamber, two stages of radiation shields and the cryostat. This permits long ion beam storage life times in the order of 1000 s. The low temperatures also provide the low radiation field, allowing most ions to cool radiatively to their internal ground states.

Figure 2.1 shows a schematic drawing of the CSR. The storage ring is quadratic in its form, with a circumference of about 35 m. In each of the four 90° corners are two 6° and two 39° deflectors as well as two focussing quadrupole families. The injected ions are produced on a 300 kV high voltage platform, which employs various types of ion sources. Within the frame of this work we used a Penning source to produce OH^+ ions. The four straight sections of CSR are used for experiments and beam diagnostics. One of the sections includes an electron cooler providing an electron beam merged colinearly with the stored ion beam. In this merged-beams configuration low collision energies down to 2 meV can be reached. The electron beam is used for further manipulation of the ion beam (electron cooling), but also as a reaction target for reactions like dissociative recombination (see Section 1). The reaction products from the electron cooler section are captured by two MCP-based detectors. The COld Movable PArticle

CounTer (COMPACT) is used to detect charged particles, and the Neutral Imaging in Cold Environment (NICE) detector is utilized for position sensitive measurements of neutral fragments and is described in detail in Section 2.3.

2.2 Neutral fragment momentum imaging

For determining the reaction rate coefficient a simple reaction product counting is sufficient, a more advanced detection technique is needed to learn about the other reaction details. This contains information about the energy balance or the involved molecular states and electron partial waves, via the kinetic energy release or the collision-angle distribution, respectively. In the merged beam experiment where the dissociated reaction products have small relative velocities compared to the center-of-mass velocity in the laboratory frame, the molecular fragments are confined on a detector downstream of the reaction zone. From the distance of the fragments at the point of detection the kinetic energy release can be determined. The relative orientation of the fragments (i.e., from the relative impact positions and times) delineates the angle between the molecular axis and the impact electron at the point of dissociation.

These variables can be derived using the imaging technique, whereby the fragments' relative velocities are reconstructed from their observed position and the arrival times on the detector. The transverse velocities can be easily calculated by measuring the fragments distance projected onto a plane detector perpendicular to the flight direction. However, only obtaining the transverse velocities is limited, as one cannot observe the full reaction kinematics of the system. This technique is called *2D imaging.* For a full kinematic picture, the position information of the two fragments must be combined with their timing information. This yields the complete distance and relative orientation between the two fragments. If both of the properties are measured simultaneously, the imaging technique is called *3D-imaging.*

Next, the basic concept of this method is described for the case of diatomic molecules. The kinematics are illustrated in Figure 2.2. The kinematics can be described as in the thesis' of A. Becker [12] and S. Novotny [14, 15]: The energy excess of a DR reaction goes partly into internal excitation of the fragments and partly into kinetic energy release E_{KER} by the two fragments, resulting in the fragment velocities $\vec{u_{i,n}}$ in the center-of-mass frame of the molecule. During DR the momentum transferred to the fragments A and B leads to the relative fragment velocity

$$v_r = |\vec{u_A} - \vec{u_B}| = \sqrt{\frac{2E_{KER}}{\mu}}, \tag{2.1}$$

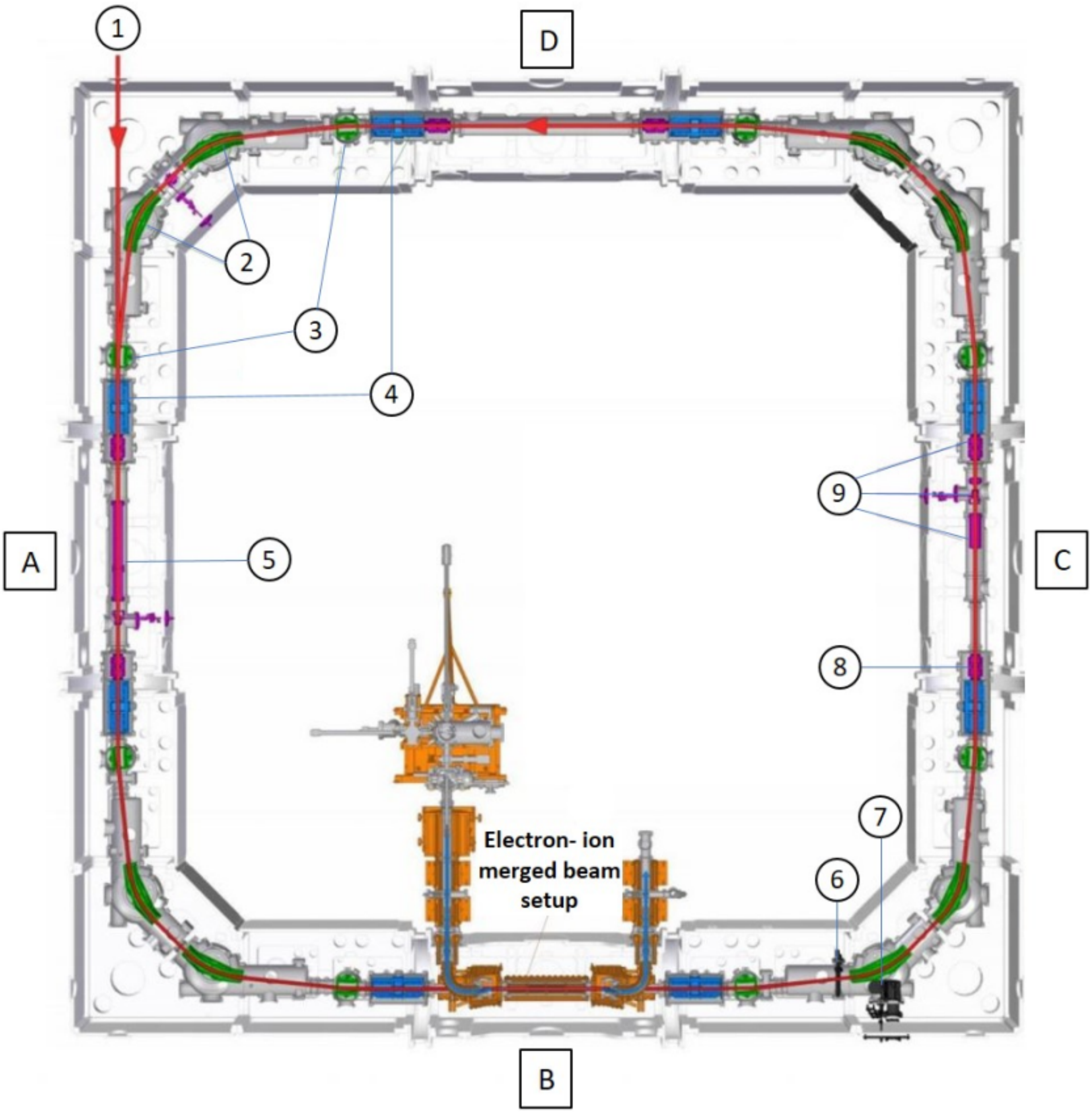

Figure 2.1: Overview of the CSR. (1) marks the injection point of the ion beam (red). It is confined to a quadratic orbit by four 90° corners. Each corner consists of two 39° (2) and two 6° deflectors (3) as well as two focusing quadrupole families (4). Four straight sections give room for experiments and beam diagnostic tools. In section (A), neutral beams can be investigated and it also includes a RF-bunching system (5). The electron cooler is located in section (B), featuring the COMPACT (6) charged particle detector and the neutral imaging detector NICE (7). Beam diagnostic tools like the position (8), the Schottky, and current pickups (9) are found in section (D). Section (D) will be equipped with a reaction microscope in the future. Adopted from [13].

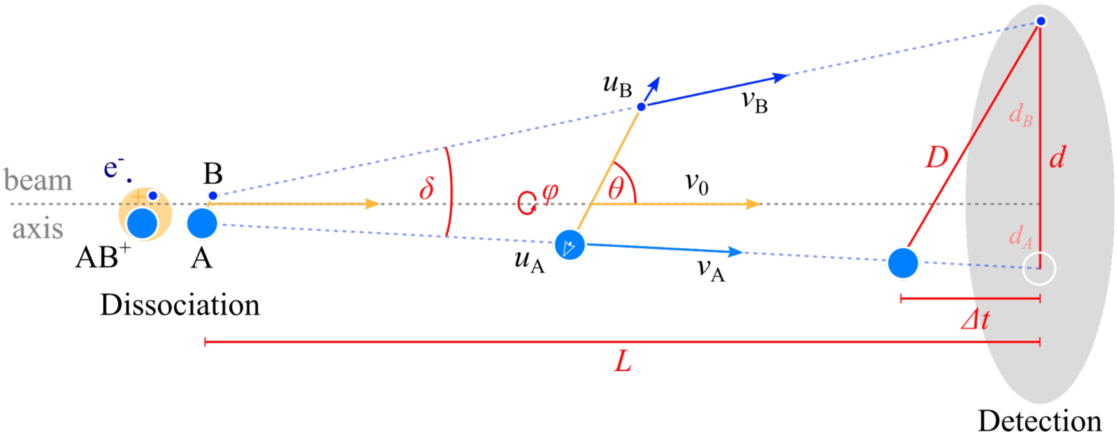

Figure 2.2: Schematic drawing of DR kinematics. An electron e^- recombines with an diatomic molecular ion AB^+. The released kinetic energy E_{KER} is transferred onto the two neutral fragments A and B propagate with the velocity v_A and v_B, respectively. In the center-of-mass frame, their velocity corresponds to the velocity of the ion beam v_0. The neutral fragments arrive on the detector with the measured transverse distance d. The faster fragment hits the detector Δt before the other one. The full distance between the two fragments corresponds to D. L describes the distance from the interaction region to the detector. Modified from [12].

where $\mu = \dfrac{m_A m_B}{m_A + m_B}$ is the reduced mass of the two fragments neglecting the momentum transfer from the electron capture. The fragments still propagate with the velocity of the ion beam v_0 in the laboratory frame:

$$v_0 = \sqrt{\frac{2E_0}{M}} \tag{2.2}$$

with kinetic energy E_0 and total mass $M = m_A + m_B$ of the stored molecular ion beam. After a time t_{TOF} the fragments reach the detector, which is at distance L from the fragmentation point. The time-of-flight t_{TOF} can be calculated from the ratio of the distance and the velocity of the fragments. As a first approximation, t_{TOF} is equal to the ratio of L and the ion beam velocity v_0 and the ratio of the 3D-distance D and the relative velocity of the fragments v_r:

$$t_{TOF} = \frac{L}{v_0} = \frac{D}{v_r}. \tag{2.3}$$

With this relation the kinetic energy release E_{KER} can be calculated as

$$E_{KER} = \frac{1}{2}\mu\left(\frac{D}{L}v_0\right)^2. \tag{2.4}$$

The molecular ions have a random orientation in the azimuth angle φ and the polar angle θ with respect to the beam axis (see Figure 2.2). The latter represents the orientation of the molecular axis at the point of dissociation. Since the dissociation times are expected to be much shorter than the rotation of the molecule, the measured dissociation angle θ gives insight in the pre-collision orientation of the molecule. Thus providing differential cross section and insight into, for example, the involvement of molecular orbitals and electron partial waves in the dissociation process.

All coordinates of a dissociation with the same E_{KER} lie on a sphere with diameter D, visible as two circles with diameter $2d_A$ and $2d_B$ on the detector plane in the center-of-mass frame. The projection of the reaction sphere onto the plane of the detector can be considered orthogonal by using the small angle approximation $D \ll L$. Therefore, the relation between the dissociation angle θ, the measured transversal distance d and the longitudinal distance Δz with the observed arrival time difference of the two fragment Δt is

$$d = D\sin(\theta) \tag{2.5}$$

$$\Delta z = D\cos(\theta) = v_0 \Delta t. \tag{2.6}$$

With those two observed distances the 3D-distance D of the two fragments can be calculated:

$$\begin{aligned} D &= \sqrt{d^2 + \Delta z^2} && (2.7) \\ &= \sqrt{d^2 + v_0^2 \Delta t^2}. && (2.8) \end{aligned}$$

From the 3D distance D the dissociation angle θ can be determined as follows:

$$\theta = \arcsin\left(\frac{d}{D}\right). \tag{2.9}$$

The kinetic energy release E_{KER} is distributed amongst the fragments according to their mass ratio. For diatomic molecules with two different nuclei, the lighter fragment has a larger relative velocity leading to a larger dissociation cone on the detector plane. The measured 2D distance d of the two fragments on the detector is the sum of the distances of both fragments $d = d_A + d_B$, as can be seen in Figure 2.2, with respect to the center-of-mass. Using momentum conservation $m_A d_A = m_B d_B$, the distance of the lighter fragment B is

$$d_B = \frac{d}{1 + \frac{m_B}{m_A}}. \tag{2.10}$$

In order to measure the full projected transverse distance, the area of the detector must be large enough. For a given detector diameter d_{max}, the limit for both fragments to be measured is

$$d_{max} = 2d_{B,max}\left(1 + \frac{m_B}{m_A}\right). \tag{2.11}$$

If this is not the case the cone of the fragment will be cut off and it is not possible to conclude on large dissociation angles θ.

2.3 The neutral fragment imaging detector NICE

The neutral fragments arising from electron-ion recombination are the main observables of dissociative recombination. In order to detect them, the Neutral fragment Imaging in Cryogenic Environment (NICE) detector is located downstream of the electron-ion merged-beam section of the CSR, the development and construction of which is described in detail in the PhD thesis of A. Becker [12]. This section gives a short insight into the structure and the functional principle of the detector, which is important in the context of this thesis.

2.3.1 Operating principle

The main components of the NICE detector are a microchannel plate (MCP) in Chevron configuration, a fast-decaying phosphor screen as the anode and a fast CMOS camera outside the cryogenic environment (see Figure 2.3). The primary detection of the neutral fragments proceeds when they impinge on the MCP. A MCP is made of a material with high electric resistance (e.g. lead glass) in which many thin, parallelly arranged channels are found. These channels are coated with photocathode material. When an energetic particle hits one of these channels, a secondary electron is emitted, which introduces an avalanche of electrons by colliding again with the channel surface. The electrons are guided through the channels by applying a high voltage across the front and back surfaces of the MCP. Due to the semiconducting nature of the channel walls, the MCP resistance increases with lower temperature, which in turn increases the recharge time of the individual channels. To counteract this, and thus to be able to measure higher possible particle rates, NICE is heated to $\sim 40\,\mathrm{K}$. For the NICE system two MCPs in Chevron configuration from PHOTONIS with a diameter of 120 mm, a thickness of 1.5 mm and a channel diameter of $25\,\mu\mathrm{m}$ are used. More specifications can be found in Appendix A.3 of A. Becker's PhD thesis [12].

The electron clouds emerging from the MCP are converted to fast-decaying light spots when they hit the phosphor screen anode, which are then observed with a high a speed CMOS-camera. Further, the electrons induce a small current pulse on the conductive layer of the phosphor screen, which can be used to deduce the timing information of the impinging particles. The phosphorescent material is P47, which has a decay time of about 100 ns from 90% to 10% of its peak intensity with a maximum light emission at 400 nm [16].

The photons generated by the phosphor screen are guided outside the cryogenic environment with a mirror and various optical elements and are then observed using a fast camera system with 512×512 pixels of 14×14 μm size and a frame rate of 1 kHz.

2.3.2 Timing readout

To understand the reaction dynamics, not only knowledge of the impact position of the neutral fragments is of importance, but also their impact time difference and with that the longitudinal distance between the fragments. Therefore, a good time resolution is needed.

As mentioned before, electron clouds emerging from the MCP induce electrical pulses in the phosphor screen anode. The pulses are capacitively decoupled from the high voltage applied on the anode and digitized with a sampling rate of 1 GHz and 8 bit resolution. The sampling rate of the digitizer limits the precision of the time information to 1 ns. The resolution of the timing information of both fragments depends on the pulse shape. If both pulses overlap too much due to a small difference in the arrival time Δt, they cannot be resolved. This issue occurs for $\Delta t \lesssim 15$ ns thus significantly limiting the 3D-imaging capability of the detector for kinetic energy releases in the electronvolt range.

For a better time resolution, the presence of a segmented anode readout on the phosphor screen would be a solution to distinguish pulses from different segments even if the time difference to the adjacent pulse is too small to be resolved in the current setup. While physical segmentation of the phosphor screen anode is technologically not convenient in the harsh CSR environment, the segmentation can also be implemented on the photon detection side employing a dedicated photon detector with a good intrinsic time resolution and multiple pixels – like a silicon photomultiplier (SiPM) array. With such a segmented time readout, impact times of separated fragments can in principle detected even at 0 ns time separation, as long as two different pixels are hit.

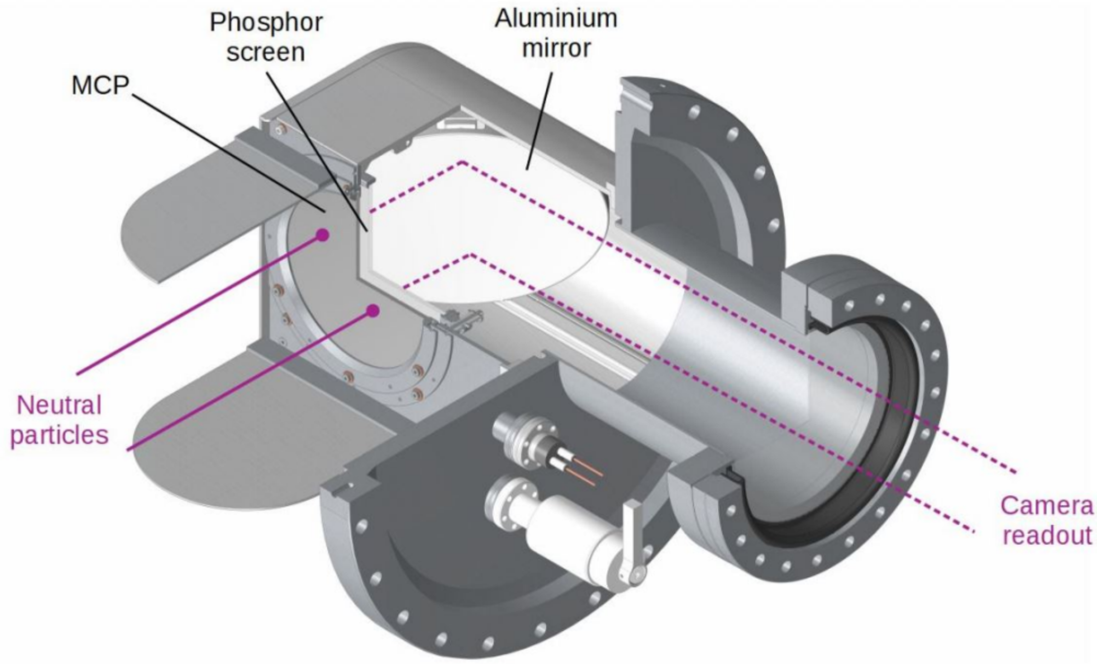

Figure 2.3: Model of the NICE detector with its main components in-vacuum parts. Neutral fragments hit the MCP, resulting in electron showers impinging on the Phosphor screen. The electrical signal induced on the Phosphor screen is used for the timing information of the detected neutral fragments. Photons generated by the electrons hitting the phosphor screen are guided outside of the cryogenic chamber through a viewport by a mirror and are imaged with a fast CMOS camera to get the position information of the neutral fragments. Based on [12].

3 A silicon photomultiplier array for timing readout of the NICE detector

The main aim of this work is to improve the 3D-imaging time resolution of the NICE detector. To realize this, we need a way to resolve the signals generated by the impact of the individual reaction products on a time scale of only a few nanoseconds. The NICE detector has various readout options, such as an electronic and an optical readout. The electronic readout uses the electronic signals from the phosphor screen anode, while the optical readout uses the photons emitted from the phosphor screen. As briefly discussed in Section 2.3.2, one possible realization of fast time readout is to use an extra detector for the light of the phosphor screen, which has multiple pixels to be able to read out the spatially separated signals independently, and thus without time resolution limit. To realize this option, we extended the already existing detection system with a silicon photomultiplier array as an additional optical readout setup.

This chapter describes the operation principle of a SiPM and introduces our SiPM array, its readout system, as well as the related data acquisition system. Further, the implementation into the existing NICE detector system is described.

3.1 Operation principle of a silicon photomultiplier

A silicon photomultiplier (SiPM) pixel is a solid-state photo detector consisting of an array of several hundred and up to several ten thousands of single-photon avalanche diodes (SPADs), called a microcell [17]. A SPAD is essentially a p-n-junction biased in reverse direction and operated above the so-called breakdown voltage.

Figure 3.1 shows the basic principle of a p-n-junction used as a photo detector in its distinct operations modes. There are three different regions of operation, which depend on the applied voltage. For a low applied voltage, the p-n-junction works in the photo diode regime. An impinging photon generates one electron-hole pair, which is separated by the applied electric field. The measured current is proportional to the light intensity. If the reversed bias voltage increases, the electric field becomes higher, so that the electrons (but not the holes) gain enough energy to create secondary electron-hole

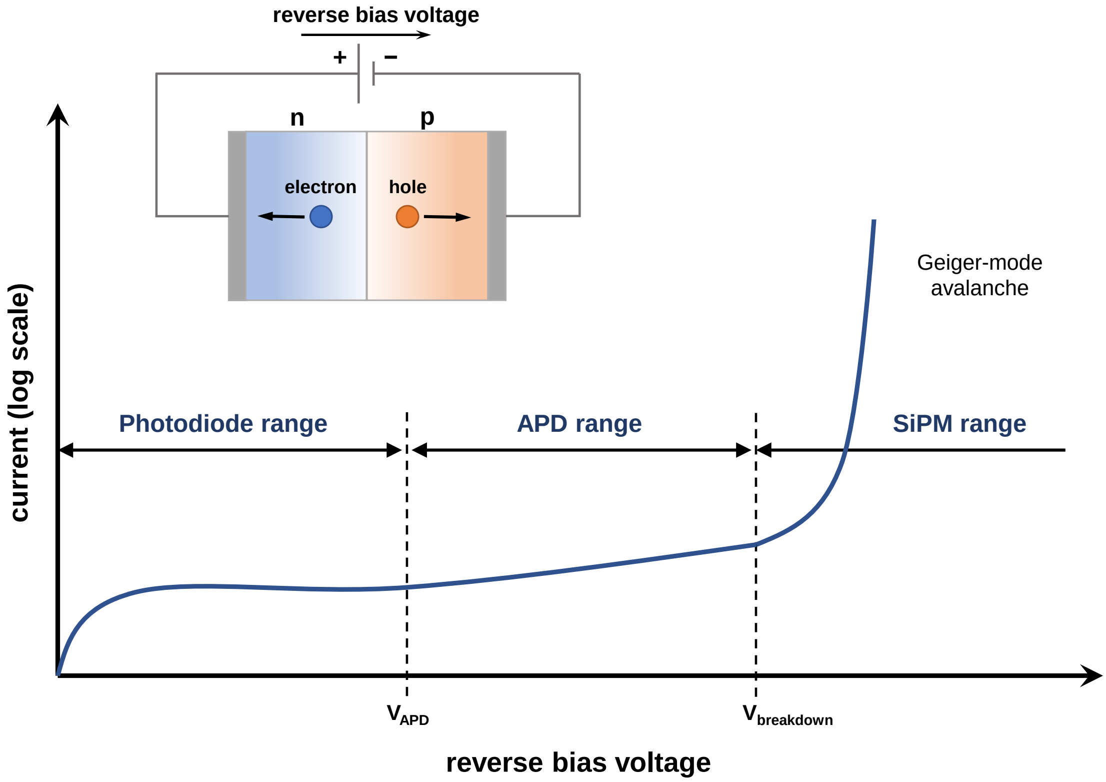

Figure 3.1: Schematic drawing of the basic principle of a p-n-junction and the operation regimes of such a device. An impinging photon creates an electron-hole pair, which is separated by the applied electrical field. The measured current depends on the operation voltage of the diode. A more detailed description can be found in Section 3.1. Modified from [18].

pairs via impact ionization. This causes an avalanche to arise, thus photo detectors operated in this voltage region are called avalanche photo diode (APD). Here the gain increases and the measured current is proportional to the number of detected photons or generated electron-hole pairs. If the reversed bias voltage is then increased above the breakdown voltage, holes will also gain enough energy to create secondary electron-hole pairs and the p-n-junction enters the region of the SPAD. Here the electric field is so high, that a single photon can trigger a self-sustaining avalanche process. This is also called Geiger mode. During this process, the measured current increases very rapidly, where the leading edge marks the arrival time of the detected photon and therefore high precision time measurements can be performed [18].

Since the avalanche is self-sustaining, the flowing current in the p-n-junction has to be stopped again. This is achieved by adding a quenching resistor to each SPAD, thereby forming a microcell together. The current flow triggered by the incident photon causes a voltage drop across the quenching resistor, which in turn causes the diode voltage to drop below the breakdown voltage, preventing further avalanches. Once the current flow has been stopped, the voltage across the diode recharges to its applied bias voltage. The time required for this process is called recovery time. It should be noted that the Geiger avalanche is confined to a single microcell, all other remain fully charged and ready to detect photons [19].

A SPAD can be constructed in two ways, either n-on-p type or p-on-n type. Which type is used depends on the wavelength of the incident photons. For shorter wavelengths (blue) the photons are absorbed closer to the surface of the diode, while long wavelength (red) photons will create electron-hole pairs deeper inside the diode [20]. The output current of the SPAD depends on the length the electrons traverse inside the diode, giving them a higher possibility to trigger an avalanche with increasing traveled length. As the generated electrons flow in the direction of the n-doped connection, due to the reverse biasing, the detection efficiency is maximized using a n-on-p diode for red light and a p-on-n type for blue light. Figure 3.2 shows a drawing of multiple microcells together as they are employed in a KETEK SiPM used in our setup (Section 3.3). It is a p-on-n diode, coated with an antireflective layer on the p-doped connection. Each SPAD has its own quenching resistor and all microcells are connected in parallel to one common cathode and one common anode output, resulting in one SiPM pixel. The SiPM signal is the superposition of all microcell signals [17].

The capability to detect and count photons with high resolution and single-photon sensitivity [22], and to obtain very good timing information on the arrival time of the detected photons [23], within several tens of picoseconds, makes the SiPM an excellent

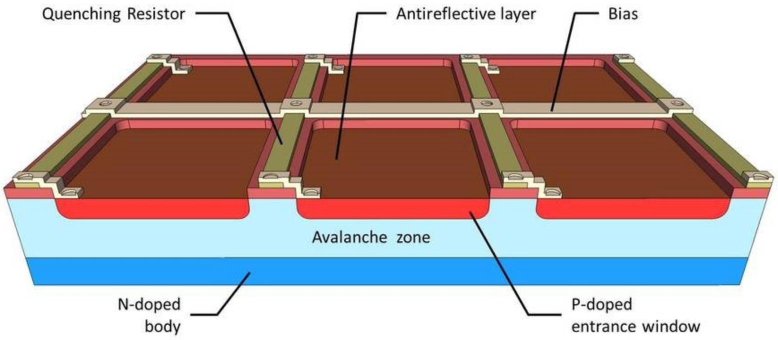

Figure 3.2: Structure of the microcells (SPADs) inside a SiPM as used by KETEK. Adopted from [21].

device for light detection. It can reliably detect single photons as well as several thousands of photons and is particularly useful when fast timing is required. Further, it is compact, robust and operates on low voltage. The latter has the benefit of simpler safety specifications, easier signal decoupling and lower costs for power supplies.

SiPM have an increasing field of application, including in light detection and ranging (LIDAR) [24], spectroscopy [25] and nuclear medical imaging. They are most commonly used for positron emissions tomography (PET), where their good time resolution is essential for time-of-flight (TOF) information [26]. SiPMs are also insensitive to magnetic fields, as opposed to photomultiplier tubes (PMTs), which makes it possible to combine PET with magnetic resonance imaging (MRI) [27]. Other advantages compared to PMTs are a higher granularity, higher photo detection efficiency (PDE), and better intrinsic timing properties [18].

3.1.1 Parameters of a SiPM

This section discusses the main parameters which describe the properties of SiMPs.

Gain

Since a SiPM is a photo diode operated in Geiger mode, the discharge of a microcell is proportional to the applied overvoltage $V_{\mathrm{OV}} = V_{\mathrm{bias}} - V_{\mathrm{breakdown}}$. The bias voltage V_{bias} denotes the voltage applied to the photo diode and the breakdown voltage $V_{\mathrm{breakdown}}$ refers to the voltage required for a p-n junction to operate in Geiger mode. The gain G is defined as

$$G = \frac{C_{\mathrm{mc}} \times V_{\mathrm{OV}}}{e} \tag{3.1}$$

with the capacity of a microcell C_{mc} and the elementary charge e.

Photon detection efficiency

The photon detection efficiency (PDE) quantifies the ability of a single-photon detector to detect photons. It is defined as the number of detected photons divided by the number of incident photons, calculated also as

$$PDE(\lambda, V_{\mathrm{OV}}) = QE(\lambda) \times \varepsilon(V_{\mathrm{OV}}) \times GE, \tag{3.2}$$

where the quantum efficiency QE describes the probability that an incident photon will create an electron-hole pair. It depends on the photon wavelength of the incident photon λ. The Geiger efficiency ε gives the probability that an avalanche is triggered and depends on the applied overvoltage V_{OV}. The geometrical efficiency GE is defined as the active area of all SPADs (microcells) divided by the total area of the SiPM pixel.

Linearity

The photon detection efficiency is linear until saturation, which is mainly limited by two factors: the number of available microcells and the recovery time of said microcells. Linear behavior over a wide range can therefore be seen in cases where the number of microcells surpasses the number of incoming photons and the recovery time is shorter than the impinging light pulses.

Noise effects

The primary noise sources of an SiPM are the dark count rate, optical crosstalk and afterpulsing.

Dark count rate Dark pulses are defined as pulses that are not triggered by impinging photons, but by thermally generated electrons. These pulses cannot be distinguished from pulses generated by detected photons. The frequency with which those pulses occur is called dark count rate. It depends on the overvoltage, because the probability of an avalanche increases with increasing overvoltage.

Optical crosstalk During each avalanche created by an impinging photon or a thermally generated electron, secondary photons are produced. About $3 \cdot 10^{-5}$ photons are generated per avalanche carrier [28] and are emitted isotropically from the fired microcell. These secondary photons can cause further avalanches in other microcells and can thus generate a signal.

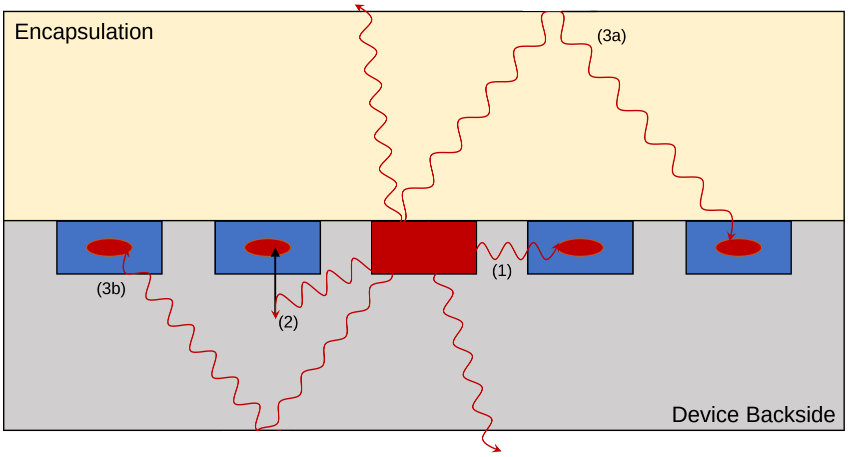

Figure 3.3: Different crosstalk paths in a SiPM pixel Modified from [29].

Figure 3.3 shows different optical crosstalk mechanisms. The most obvious one is *direct optical crosstalk* (1). Here, the secondary photons travel directly to a neighbouring cell and triggers an avalanche. The secondary photons can also generate an electron-hole pair close to a microcell, which then diffuses to it, releasing a discharge. This is called *delayed optical crosstalk* (2). Another type of crosstalk is *external crosstalk* (3 a,b). Since the secondary photons are emitted isotropically, a large part will exit via the active side of the SiPM. They can be reflected at one of the interfaces like the encapsulation (3a) or the SiPM backside (3b). As a result, external crosstalk is not restrained to neighbouring microcells anymore.

Afterpulsing Afterpulsing describes the effect that charge carriers can be trapped in the high-field region during the avalanche creation in a microcell. Their release can happen during a period of up to several μs [29] triggering another seemingly unconnected avalanche.

3.2 Optical setup

Up until this section, we have discussed the operation principle of the SiPM and the parameters commonly used to characterize it. From this section onwards, we will focus on our setup specifically and go into detail on the most important steps we took to extend the detection system. To use a SiPM array in the existing setup of the NICE detector (see Chapter 2.3), an expansion of the optical readout setup was necessary. For that purpose we designed and commissioned a new optical table. On it one can still find the high-speed CMOS camera for transverse impact position readout (see Chapter 2.3) as well as a videocamera, which is used as a first instance to check on the detection setup visually. To include an SiPM array for time readout, a larger optical table had to be designed and commissioned so that it would be possible to image the whole phosphor screen on the area of the SiPM array.

Figure 3.4 shows a schematic drawing of the optical elements used for reading out the position and time information of the impinging neutral fragments on the MCP inside CSR, in scale. The photons emitted by the phosphor screen are guided outside the cryogenic environment by a aluminum mirror through an optical view-port. Mounted to the CSR outer wall is the optical table, which is surrounded by a light-tight box. In front of the view-port a high-speed CMOS camera is positioned next to a $50\,\mathrm{mm} \times 50\,\mathrm{mm}$ plate beam-splitter with a transmission-reflection ratio of 50:50. Part of the photons are observed by the videocamera located behind the beam-splitter. The other part of the photons traverse a $2''$ bi-convex lens with a focal length of $250\,\mathrm{mm}$ and are focused on the SiPM array plane. At this point it should be emphasized that the SiPM array is not equipped with any built-in lens, and thus the light is focused directly on the SiPM's active area.

In first approximation, the requirements for the optical readout system can be calculated by using the thin lens approximation. When a lens is used to form an image of an object, the distance from the object to the lens g, the distance from the lens to the image b, and the focal length f are related by the lens equation

$$\frac{1}{f} = \frac{1}{g} + \frac{1}{b}. \tag{3.3}$$

The magnification factor $\beta = \frac{B}{G} = \frac{b}{g}$ gives the ratio between the object size G and the image size B. With β and Eq. 3.3, the distance of the lens to the image b or object g can be estimated:

$$b = (\beta + 1) f \tag{3.4}$$

$$g = \left(\frac{1}{\beta} + 1\right) f. \tag{3.5}$$

With a phosphor screen of size (126 mm) and a SiPM array of size (55 mm) the magnification factor is $\beta \approx 0.44$. Therefore, the distance from the phosphor screen to the lens is calculated to be $g = 818\,\mathrm{mm}$ and the distance from the lens to the SiPM array plane should be $b = 360\,\mathrm{mm}$. For a better visualization of the optical path through the various

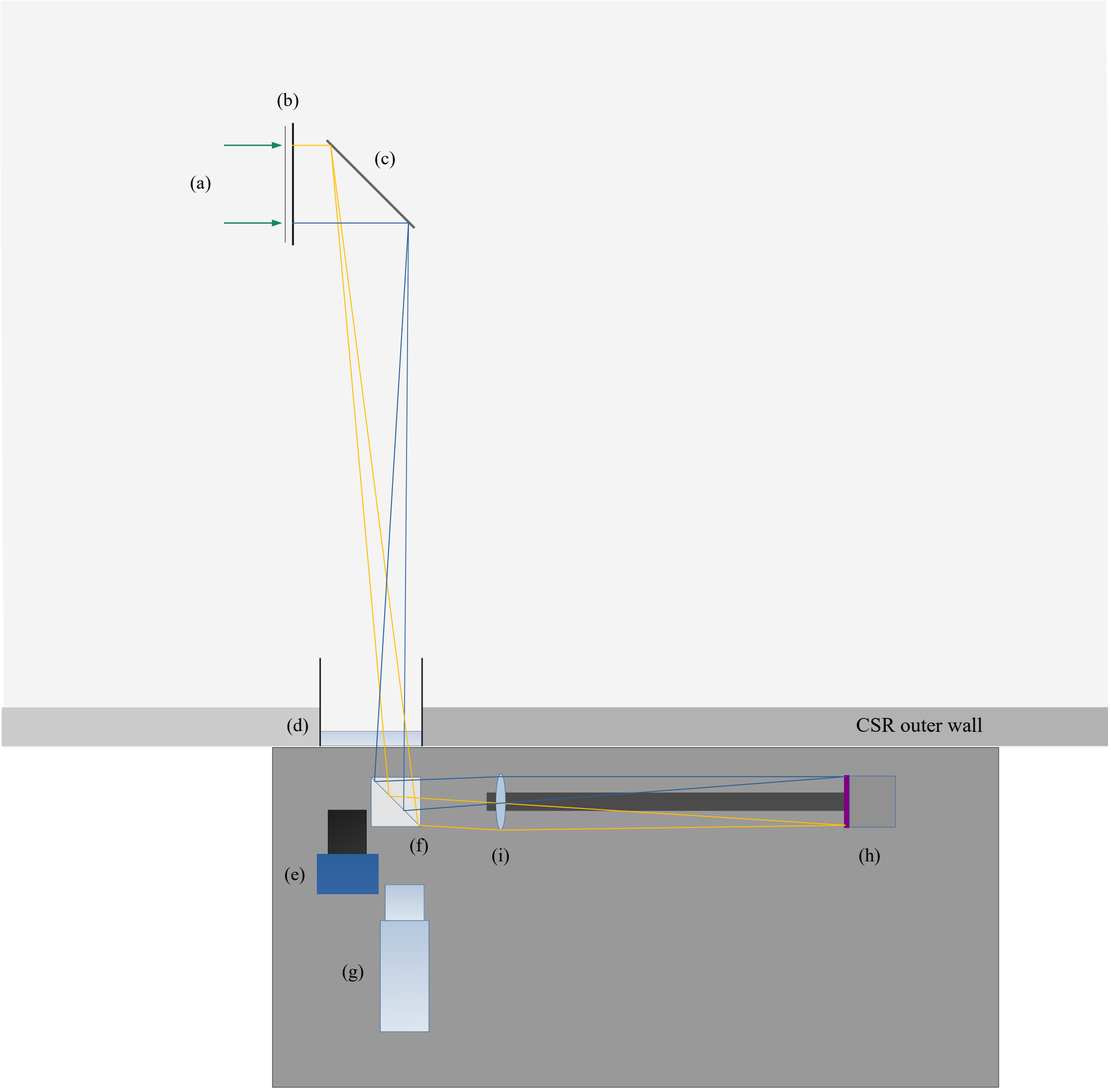

Figure 3.4: Schematic drawing of the optical readout setup including the SiPM array (top view). Particles (a) impinging on the MCP & phosphor screen setup (b) generate photons, which can be observed from outside the cryogenic environment at a 90° angle via an aluminum mirror (c) and view-port (d). Mounted to the view-port is an optical table surrounded by a light-tight black box. In front of the view-port is a high-speed CMOS camera (e) used for imaging and a beam-splitter (f) that guides half of the photons to a videocamera (g) and the other half to the SiPM-setup (h). The SiPM array is illustrated in purple; the gray box marks its read-out electronics. A focusing lens (i) and the SiPM setup are mounted on an optical rail for easy alignment and adjustment.

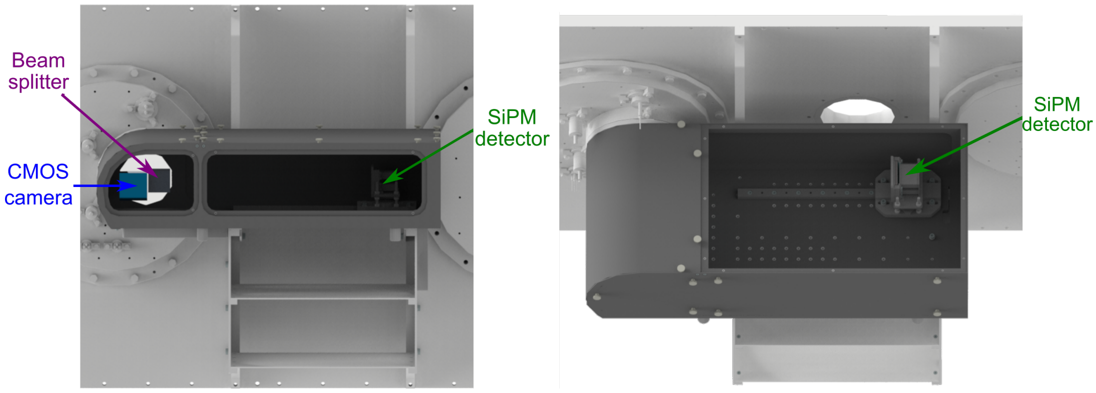

(a) Model of optical table with open side (b) Model of optical table with open top

Figure 3.5: Model of the new optical table with surrounding light tight box mounted to the outer wall of the CSR. The optical elements can be easily accessed by removing part of the box-cover. It can be opened from the side (a) to access the optical elements in front of the viewport. The straight part on the top can also be removed to fully access the SiPM setup (b). Underneath the optical table are also two additional shelfs for the readout electronics and the power supply.

optical elements, we used the geometrical optics simulation software Optgeo [30] and determined the current setup (shown in Figure 3.4) to be the most efficient. Based on those dimensions the new optical table was designed. It has a size of 750 mm × 350 mm and is surrounded by a light tight box. To fix the optical elements on the table, threaded holes with a pitch of 25 mm in front of the view port and along an optical rail leading to the SiPM array are embedded into the optical table. On the area where no optical elements are placed (see Figure 3.4) the pitch of the holes is 50 mm. The optical elements inside the box are easily accessible, because the box can be opened on different sides, as can be seen in Figure 3.5.

The optical readout setup is spacious enough so that it can be extended by additional lenses and a mirror in such a way that the full size of the SiPM array would image a part of the phosphor screen and therefore to zoom in part of the phosphor screen detector area.

3.3 The KETEK SiPM array

The from now on called SiPM detector, as it is implemented in the optical setup of the NICE detector (see Section 3.2), consists of four SiPM arrays of the type KETEK PM3325-WB-0808 [17] arranged quadratically in a 2 × 2 orientation (see also Fig B.1 in

Table 3.1: Properties of the KETEK PM3325-WB-D0 single pixel operated with an overvoltage of $V_{\mathrm{OV}} = 5\,\mathrm{V}$ at 21°C [31].

Parameter	Typ. @ 5.0 V_{OV}
Breakdown Voltage $V_{\mathrm{breakdown}}$ at 21°C	min. 24.0 V, max. 25 V
Temperature Dependency of $V_{\mathrm{breakdown}}$	22.0 mV/K
Gain	1.74×10^6
PDE	45%
Dark Count Rate	125 kHz/mm^2
Dark Current	0.7 μA
Crosstalk Probability	26%
including delayed crosstalk probability	<0.1%
Afterpulsing Probability	5%
Recovery Time τ	33 ns (at 1 Ω load) 80 ns (at 50 Ω load)
Signal Rise Time	110 ps

Appendix B)).

Each of the four arrays consists of 8×8 pixels, each based on the single-pixel model KETEK PM3325-WB-D0 [31]. Each pixel has an active area size of $3 \times 3\,\mathrm{mm}^2$ comprising 13920 microcells with a size of 25 μm each. The pitch between pixels in one array is 3.36 mm, resulting in an array size of $26.84 \times 26.84\,\mathrm{mm}^2$ including a frame of 0.16 mm, edging the array, and a thickness of 5.21 mm. We operated the array at a breakdown voltage of $V_{\mathrm{breakdown}} = 24.7\,\mathrm{V}$ with an overvoltage $V_{\mathrm{OV}} = 2\,\mathrm{V}$. Typical values for the parameters of a single KETEK SiPM pixel are summarized in Table 3.1.

When the four arrays are combined to form the SiPM detector, we have 16×16 pixels in total. Its covered area is $54.34 \times 54.34\,\mathrm{mm}^2$, with a small gap of 0.7 mm between the arrays due to their attachment to the SiPM readout electronics.

3.4 SiPM detector setup

The readout electronics and core of the data acquisition system of the SiPM detector is a commercial solution by PETsys Electronics.

The SiPM detector comprises four arrays, two of each connected to one Front-End-Module (FEM), respectively. The FEMs are the interface between the analog signals of the SiPM and the digital readout chain. They are directly connected to the SiPM arrays and are therefore also inside the optical box on the SiPM holder (see Figure 3.6). Each FEM has an TOFPET2 Application-Specific Integrated Circuit (ASIC), developed

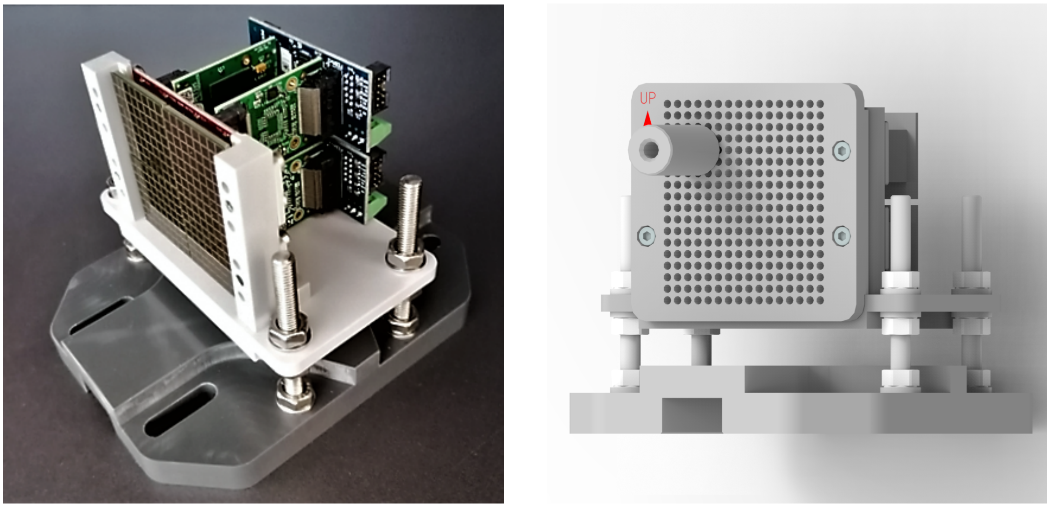

(a) Holder of the SiPM detector and part of its readout electronics (FEM boards).

(b) Holder of the SiPM as in (a) with attached calibration mask and LED holder.

Figure 3.6: Photograph of the SiPM detector including FEM boards and its holder (a). The holder is adjustable in height with four screws and can be placed upon an optical rail. In front of the SiPM array a calibration mask can be attached and an LED holder can be inserted for single pixel illumination (b).

by PETsys, on which the SiPM readout system is based. A temperature sensor is also a placed nearby to monitor the temperature of each ASIC during its operation. The TOFPET2 ASIC is a 64 channel chip optimized for readout and digitization of signals from SiPMs in applications with high data rate and fast timing requirements. For each channel (i.e., each SiPM pixel) three different thresholds can be set. A low threshold ($t1$) for timing, a second threshold ($t2$) for rejecting dark counts and an energy threshold (E) for validating the event. Only events that pass all three thresholds are digitized and evaluated in terms of trigger time and pulse height or pulse area [32].

Both FEMs are connected with flexible coaxial flat Samtec cables to the Front-End-Board (FEB/D), providing flexibility in the experimental setup. The FEB/D provides power for the ASIC and the SiPM arrays, hosts a clock & trigger unit with a 200 MHz clock, and conducts the communication to the DAQ computer via an ethernet cable (Figure 3.7). The FEB/D board can also accept an external signal. This can be used for synchronization purposes with an external DAQ system.

The DAQ computer (SiPM-PC) configures the TOFPET2 parameters and the bias voltages and thus controls the acquisition. This is done with Python scripts provided by PETsys or a graphical user interface (GUI) based on those scripts. The SiPM bias

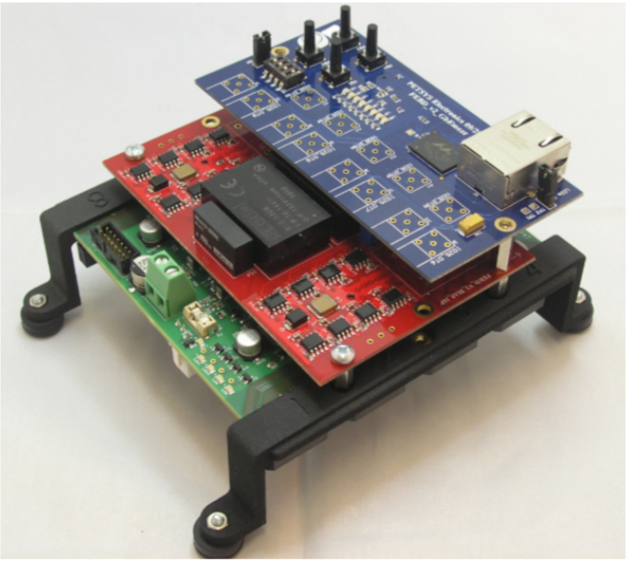

Figure 3.7: Photograph of the FEB/D board with its 3 floors in green, red and blue [33].

setting are set corresponding to the parameters given by the SiPM array manufacturer. For the KETEK PM3325-WB-0808 arrays the values can be found in Section 3.3. Before a measurement can be started, the system needs configuration and calibration files. The configuration files are required for data acquisition and calibration files are used to obtain correct time and charge stamps for each event from the raw data provided by the ASICs. This is done by calibrating the involved analog-to-digital converter (ADC) circuits, time-to-digital converters (TDC) circuits, and discriminator thresholds at the specific voltages and temperature. All the relevant files and parameters are referred to in a single file called "config.ini". Certain ASIC parameters, like the scaling of the threshold values and the gain, can be modified in it directly. It should be mentioned here, that acquiring a calibration is not required every time one starts a measurement, but only if the SiPM or ASIC parameters are changed, or the ASIC operation temperature varies by more than 5°C. For our setup, temperature stabilization around 25°C is reached in about ten minutes after switching on the electronics in a beamtime. We observed temperature changes when starting the stabilization during cool-down and warm-up of the CSR due to the changes in room temperature.

The configuration file also refers to a channel map, which assigns to each pixel an x_i and y_i geometric position value specific for the SiPM array orientation in our detector. These coordinates propagate to the acquired data for each triggered SiPM pixel. More details on the channel map can be found in Appendix B.

The acquisition on the SiPM-PC can run in a stand-alone mode where the user decides the start and end of the time of acquisition. For the practical use with the general CSR data acquisition system (CSR-DAQ) the acquisition can be controlled remotely, using a TCP/IP server interface. A simple communication protocol allows to start and stop the acquisition and to set a file name. It is also possible to separate files per injection cycle. The main CSR-DAQ can thus synchronize the SiPM acquisition with the global measurement.

During data acquisition multiple variables are recorded per event and stored to output files. This includes the timestamp of an event, in which pixel of the SiPM detector the signal was registered, identified by a uniquely assigned global channelID, and the energy of the event. All acquired variables are listed in Table C.1 in Appendix C.

The acquired raw data output from the SiPM setup contains only the measured values from the ASICs' ADCs and TDCs in ADC units. For data analysis, these values have to be converted to time and energy using the acquired calibration files. This data processing is done with scripts provided by PETsys.

It is also possible to convert the raw data into ROOT-files. Within the ROOT data framework the class TTree is used to structure the variables [34]. A ROOT Tree can loosely be described as a table, where the table has as many rows as there are entries (in our case the number of events) and branches corresponding to columns representing some property of the event (e.g., time). The full structure of the data Tree is shown in Table C.1 in Appendix C. This data format is convenient for rapid data analysis and projections.

3.5 Inter-pixel time calibration

The different TOFPET2 ASIC channels, and with that the different pixels, have an intrinsic time offset of about 5 ns. To correct the acquired data for this offset, we performed an inter-pixel time calibration.

To achieve uniform illumination of all pixels of the SiPM detector simultaneously we used short LED pulses with an LED of the type LED465E by Thorlabs and two diffusers. Diffuser 1 is a 2" N-BK7 ground glass diffuser with 120 Grit and diffuser 2 is a 2" N-BK7 ground glass diffuser with 220 Grit, both manufactured by Thorlabs.

We arranged the elements in the following way: The plane of the SiPM detector was used as the reference point. A neutral density filter with an optical density of $OD = 1.3$ was mounted to the holder of the SiPM directly in front of the detector plane covering the whole active area of the detector. Diffuser 1 was placed at a distance of 170 mm in relation to the detector plane. Connected with a black 2" tube, diffuser 2 was located 235 mm away and the LED was positioned at a distance of 310 mm to the detector plane.

Using the full illumination of the SiPM detector, we performed a inter-pixel time calibration. For that purpose, we acquired data for 10 s per pixel. The LED was operated with a voltage of 8.4 V and emitted 5 ns pules at a rate of 100 Hz, resulting in 1000 pulses over the course of 10 seconds. These pulses were used for the inter-pixel time calibration of each pixel. The pulses generated for the LED were also fed into the SiPM electronics as a reference time signal. It was assigned to the channel with global $channelID = 17$, corresponding to the bottom leftmost pixel, which was therefore not able to acquire photons emitted from the LED. For this measurement we changed the scaling of the thresholds from the default value. The following parameters of the main configuration file "config.ini" were changed to:

- $global.disc\_lsb\_t1 = 62$
- $global.disc\_lsb\_t2 = 56$
- $global.disc\_lsb\_e = 53$,

which represent the scaling factors of the analog signal before digitization in the TOFPET2 ASIC, for the respective threshold pipelines. The thresholds for the acquiring pixel were set to $t1 = 10$, $t2 = 5$, and $tE = 3$. With these parameters we were able to approximately mimic the light intensity and pulse duration from the LED corresponding to the light pulses from the phosphor screen. For the inter-pixel time calibration it was important to acquire the LED signals only with one pixel. Illuminating all pixels with the LED at the same time resulted in a saturation of the ASIC processing capabilities. To be able to acquire the LED signals with a single pixel, we set the thresholds of all other pixels to $t1 = 60$, $t2 = 60$, and $tE = 60$ so that no signals were recorded in the other pixels.

The acquired data was processed for further analysis using a *grouping algorithm*, which groups recorded hits on the SiPM detector to one event, i.e. one LED pulse in this test. We make the assumption, that all hits seen in a time window of $1\,\mu s$ belong to the same main event and are therefore put in one group. When discussing an event in the following, such a group of hits is implied.

To perform the inter-pixel time calibration we used output values of the grouping algorithm. In the grouping algorithm the delay time tD in general describes the time for every hit with respect to the first hit in one event. Since we only measured at most two hits, tD refers to the time of the LED signal and $tD[tRI]$ to the delay time of the

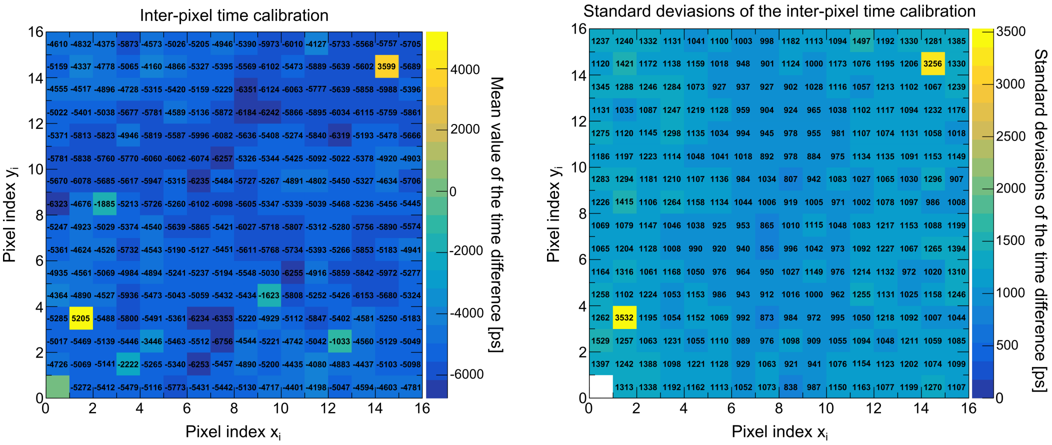

-4610	-4832	-4375	-5873	-4573	-5026	-5205	-4946	-5390	-5973	-6010	-4127	-5733	-5568	-5757	-5705
-5159	-4337	-4778	-5065	-4160	-4866	-5327	-5395	-5569	-6102	-5473	-5889	-5639	-5602	3599	-5689
-4555	-4517	-4896	-4728	-5315	-5420	-5159	-5229	-6351	-6124	-6063	-5777	-5639	-5858	-5988	-5396
-5022	-5401	-5038	-5677	-5781	-4589	-5136	-5872	-6184	-6242	-5866	-5895	-6034	-6115	-5759	-5861
-5371	-5813	-5823	-4946	-5819	-5587	-5996	-6082	-5636	-5408	-5274	-5840	-6319	-5193	-5478	-5666
-5781	-5838	-5760	-5770	-6060	-6062	-6074	-6257	-5326	-5344	-5425	-5092	-5022	-5378	-4920	-4903
-5670	-6078	-5685	-5617	-5947	-5315	-6235	-5484	-5727	-5267	-4891	-4802	-5450	-5327	-4634	-5706
-6323	-4676	-1885	-5213	-5726	-5260	-6102	-6098	-5605	-5347	-5339	-5039	-5468	-5236	-5456	-5445
-5247	-4923	-5029	-5374	-4540	-5639	-5865	-5421	-6027	-5718	-5807	-5312	-5280	-5756	-5890	-5574
-5361	-4624	-4526	-5732	-4543	-5190	-5127	-5451	-5611	-5768	-5734	-5393	-5266	-5853	-5183	-4941
-4935	-4561	-5069	-4984	-4894	-5241	-5237	-5194	-5548	-5030	-6255	-4916	-5859	-5842	-5972	-5277
-4364	-4890	-4527	-5936	-5473	-5043	-5059	-5432	-5434	-1623	-5808	-5252	-5426	-6153	-5680	-5324
-5285	5205	-5488	-5800	-5491	-5361	-6234	-6353	-5220	-4929	-5112	-5847	-5402	-4581	-5250	-5183
-5017	-5469	-5139	-5446	-3446	-5463	-5512	-6756	-4544	-5221	-4742	-5042	-1033	-4560	-5129	-5049
-4726	-5069	-5141	-2222	-5265	-5340	-6253	-5457	-4890	-5200	-4435	-4080	-4883	-4437	-5103	-5098
	-5272	-5412	-5479	-5116	-5773	-5431	-5442	-5130	-4717	-4401	-4198	-5047	-4594	-4603	-4781

1237	1240	1332	1131	1041	1100	1003	998	1182	1113	1094	1497	1192	1330	1281	1385
1120	1421	1172	1138	1159	1018	948	901	1124	1000	1173	1076	1195	1206	3256	1330
1345	1288	1246	1284	1073	927	937	927	902	1028	1116	1057	1213	1102	1067	1239
1131	1035	1087	1247	1219	1128	959	904	924	965	1038	1102	1117	1094	1232	1176
1275	1120	1145	1298	1135	1034	994	945	978	955	981	1107	1074	1131	1058	1018
1186	1197	1223	1114	1048	1041	1018	892	978	884	975	1134	1135	1091	1153	1149
1283	1294	1181	1210	1107	1136	984	1034	807	942	1083	1027	1065	1030	1296	907
1226	1415	1106	1264	1158	1134	1044	1006	919	1005	971	1002	1078	1097	986	1008
1069	1079	1147	1046	1038	925	953	865	1010	1115	1048	1083	1217	1153	1088	1199
1065	1204	1128	1008	990	920	940	856	996	1042	973	1092	1227	1067	1265	1394
1164	1316	1061	1168	1050	976	964	950	1027	1149	976	1214	1132	972	1020	1310
1258	1102	1224	1053	1153	986	943	912	1016	1000	962	1255	1131	1025	1158	1246
1262	3532	1195	1054	1152	1069	992	873	984	972	995	1050	1218	1092	1007	1044
1529	1257	1063	1231	1055	1110	989	976	1098	909	1055	1094	1048	1211	1059	1085
1397	1242	1388	1098	1221	1128	929	1063	921	941	1076	1154	1123	1202	1074	1099
	1313	1338	1192	1162	1113	1052	1073	838	987	1150	1163	1077	1199	1270	1107

Figure 3.8: Inter-pixel time calibration. The values plotted in each pixel correspond to the mean time difference (a) between the LED signal and the reference pulse. The standard deviation of the mean values, seen in (b), is used as errors in the inter-pixel calibration. The time information is given in ps in both plots.

reference pulse. We then subtracted $tD[tRI]$ from the delay time tD for each event in one pixel. The mean value of this subtraction is used as an timing offset between the different pixel. This is illustrated in Figure 3.8, showing pixel maps of the SiPM detector. In panel (a) the mean value of the difference of the delay times tD of the hits to the delay time of the reference pulse $tD[tRI]$ are displayed. Overall, the time difference between the hits and the reference pulse are uniformly except for two pixels at $(1|4)$ and $(14|15)$. For those two the difference of the timing information of the pulses and the reference are positive, meaning that the LED signal arrived about 3.6 ns to 5.2 ns after the reference pulse. For all other pixels the signal of the reference pulse was measured later than the LED pulse. The mean time difference between the reference pulse and the LED signal ranges from −1.0 ns to −6.8 ns. On average the mean value of the time difference for all pixels, except the two corrupted ones, is −5.3 ns. For the same two pixels the standard deviation of the mean value is also approximately three times higher than for the other pixels, shown in Figure 3.8 (b). For the data discussed in this thesis, the two corrupt pixels are not relevant, as the phosphor screen is not imaged on them.

The time offsets obtained in the inter-pixel calibration procedure were used to correct the pixel trigger times in other datasets.

3.6 Synchronization of the SiPM setup with the CSR-DAQ

The NICE detector has multiple readout option, like the SiPM detector, the fast CMOS-camera and the digitized anode signal of the MCP & phosphor screen setup. The later two are handled by the main CSR-DAQ system and are synchronized in an independent procedure, which is beyond the scope of this work. The SiPM readout, driven by the SiPM-DAQ, is running asynchronously from the CSR-DAQ and therefore an additional mechanism for the assignment of the acquired events from the two acquisition systems is needed. This is done based on timing information from the events recorded by the SiPM detector and by the already synchronized CSR-DAQ events, taking the timing information from the digitized anode signal.

The time stamps in both data acquisition systems are based on different hardware clocks. The overall data acquisition system CSR-DAQ controls several hardware components, including a field programmable gate array (FPGA), which takes care of the timing with a 10 MHz clock. The time stamps of the events are based on this clock. Similarly, for the SiPM system the internal 200 MHz clock provides the event times. Both of these independently acquired time-stamps need to be synchronized to correctly assign the events. The synchronization needs to be carried out in terms of the clock frequency scaling, and in the time-zero offset. For the offset, the time of the previous ion injection is used, so that the corrected time value directly corresponds to the ion storage time.

For this purpose, every 100 ms a regular synchronization pulse is sent from the FPGA to the SiPM detector. It is fed into the readout electronics and can be accessed in the processed data file as trigger times of one selected channel. When a new ion injection cycle is started, the time of injection is also marked with a synchronization pulse and with an additional synchronization pulse pattern, i.e. the injection pulse is followed by a synchronization pulse after 10 ms and another one after 20 ms with respect to the 10 ms-pulse. Afterwards, the regular 100 ms pulse pattern continues. The fact that the synchronization pulses are generated by the CSR-DAQ clock, but the measured times of the synchronization pulses are based on the SiPM clock allows for the clock frequency synchronization. The special pattern after the injection can be used to synchronize the absolute storage times in the two systems.

On the software side, we used an offline synchronization script based on the ROOT framework, especially the TTree class [34]. For someone not familiar with ROOT Trees, they can loosely be described as tables, where the table has as many rows as there are entries (in our case the number of events) and one branch corresponds to a column representing some property of the event (e.g., time).

The synchronization is fundamentally based on the comparison of the storage times, i.e. the time that has passed after the injection, of events recorded with the SiPM-DAQ and with the CSR-DAQ. We note that the absolute times of the SiPM records have an arbitrary offset, which is not related to the experiment. To convert them to the storage time domain, we determine the time of injection by the pattern of external pulses described above and subtract this value from the time of the SiPM-DAQ event. The storage time of SiPM-DAQ events in denoted by $tstor$-branch, whereas the storage time of the CSR-DAQ events, having their time information from the digitized pulses of the anode, are called Cam_t. The algorithm goes from event to event in the CSR-DAQ event tree and tries to match it with a recorded event from the SiPM detector. First, the algorithm checks whether the event in the SiPM is an external synchronization pulse or not. If yes, it computes a calibration factor C, which is a factor for the scaling between the CSR-DAQ and SiPM-DAQ clocks.

For this purpose the time after injection $tstor$ for each synchronization pulse in the SiPM clock is compared to the expected storage time T in the domain of the CSR-DAQ clock. The T value is easily determined from the count of the synchronization pulses after previous injection and the known 100 ms period of the synchronization pulses in the CSR-DAQ time domain. The, dividing the found target value T by the measured value in the SiPM-DAQ domain $tstor$ gives us then the calibration factor $C = T/tstor$. With it the storage time of the SiPM events is corrected, applying a linear function:

$$tstorC = tstor \times C + O. \tag{3.6}$$

The offset O is a constant-value delay between the injections signals as propagated to the two DAQ systems ($\sim$ 1 ms), and its value is evaluated before the start of the synchronization by matching the first few events manually.

The times of the other data entries from the detector impacts can also be synchronized with the derived C and O parameters. The corrected storage time of the SiPM event $tstorC$ is then compared to the storage time of the CSR-DAQ Cam_t. If it lies within a window of ±250 ns, the events are matched. In case an event in the CSR-DAQ was not able to be matched with any event in the SiPM detector, the CSR-DAQ event is labelled with a flag $nosync = -1$. If the event was synchronized, $nosync = 0$. Typically about 3% of the CSR-DAQ events do not have any synchronized SiPM events. One possible origin of such cases can be low-intensity light pulses hitting non-sensitive parts of the SiPM array between the pixels. For debugging purposes, the time difference $tdiff$ between the the closest not synchronized SiPM event and CSR-DAQ event are also recorded. This procedure is executed for each event in the CSR-DAQ. The output ROOT-file for one run contains a TTree structure as explained in Table 3.2. The events in the output TTree are now synchronized with the data of CSR-DAQ by the record index. Therefore, the SiPM, anode-signal, and CMOS camera data can be easily combined.

Table 3.2: Output variables of the synchronization script between SiPM events and CSR-DAQ events. The variables correspond to branches of the Tree structure in the output ROOT-file.

Quantity/ Variable	Data type	Unit	Comment
Cam_t	Long64_t	ns	Storage time of CSR-DAQ events (from digitizer)
tC	Int_t		ChannelIDs for pixels in the SiPM event
tt	Long64_t	ps	Timestamp of the SiPM event using internal clock
tN	Uchar_t		Number of pixels responding within one SiPM event
nosync	Int_t		Flag if CSR-DAQ event was synchronized or not (0|-1)→ (yes|no)
C_1	double		C-1 (Time calibration factor subtracted by -1)
C	double		Time calibration factor between the FPGA and SiPM clock
tdiff	Long64_t	ns	Time difference between closest not synchronized SiPM event to CSR-DAQ event
tD[tN]	Long64_t	ps	Delays within the event with respect to first responding pixel in SiPM detector
tRI	Int_t		Index of the reference channel, -1 if not present in this event
tE[tN]	Float_t		Energy for each pixel in SiPM event
txi[tN]	Int_t		X-coordinate index for each pixel in SiPM event
tyi[tN]	Int_t		Y-coordinate index for each pixel in SiPM event
tstorC	Long64_t	ns	Calibrated storage time of SiPM detector

4 Experiemental results

The previous chapter introduced an extension of the NICE detection setup, which enables us to perform 3D-imaging of the products from dissociative recombination of molecular ions and electrons with a better time resolution, employing the SIPM array technology. The following chapter describes the performance of this new detection technique, which was first tested during the OH^+-beamtime at the Cryogenic Storage Ring in February 2021.

During the beamtime, we tested the basic working principle as well as the performance. At this point we want to emphasize again, that the main goal of this setup is to improve the time resolution of the neutral fragment imaging detector NICE, i.e., its ability to resolve the particle impact times even if the impacts occur close in time, as well as the precision of the derived impact times.

In this chapter, we first give a short introduction into the OH^+ DR experiment. Then, we take a look at the performance of the SiPM detector with regard to the events acquired with the CSR-DAQ system. and compare the timing information acquired of the SiPM-detector and the digitized anode signal employed in the CSR-DAQ. Everything discussed below assumes synchronized SiPM and CSR-DAQ data (see Section 3.6).

4.1 OH^+ DR measurements

During the beamtime at the Cryogenic Storage Ring in February 2021 we performed dissociative recombination (DR) measurements of the diatomic molecular ion OH^+. This was the first time we used the newly implemented SiPM detector coupled to the CSR-DAQ and tested its performance.

Measurement parameters

To perform the measurements, we injected OH^+ ions with an acceleration voltage of $\sim 280\,\mathrm{keV}$ into the CSR and employed electron cooling line here [8]. Multiple measurement-runs were acquired, varying in the structure of the electron-ion collision energy pattern versus ion-storage time.

The results presented in this chapter focus on an image intensive run, which provides high statistics and consists of 20 injection cycles in total. After each ion injection, the measurement was structured in three different schemes, where each scheme consists of various measurement steps. In each step, the electron-ion collision energy is set to a required value by tuning the electron beam velocity in the laboratory frame. In the measurement run used here, electron cooling at 0 eV electron-ion energy was applied for $\sim$ 100 ms after ion injection. This was followed by $\sim$ 100 ms of storage with the electron beam being switched off. In the third scheme, the electron-ion collision energy was varied in the multiple steps, though in 2/3 of the time the 0 eV cooling step was applied to keep the phase-space electron cooling. A more detailed description of the measurement schemes employed in the OH+ DR experiment is beyond the scope of this work.

To test the performance of the SiPM detector, we only focus on the cooling step in scheme number three. For each injection, the measurement time of the cooling step accumulates to $\sim$ 40 s with a total storage time of $\sim$ 220 s. As mentioned, the collision energy in the cooling step is 0 eV. At these conditions there is no preferred collision angle between the molecular axis and the electron impact vector. Therefore, also the detected azimuth angle φ and the polar angle θ between the DR fragments with respect to the beam axis will be randomized.

Detector settings

The detection of the neutral fragments resulting from DR reaction was done using the NICE detector including the SiPM readout. As described in Section 2.3.1, the main detection system of the NICE detector is an MCP with a phosphor screen anode. The MCP front was lifted to a potential of $-1100\,\mathrm{V}$, while the back surface was kept at $+678\,\mathrm{V}$. Following this, the phosphor screen was kept at $+10500\,\mathrm{V}$ to attract the emerging electron cloud, which produces a short-lived bright spot that can be observed by both the fast CMOS camera and the SiPM detector.

During the OH^+ measurements, the SiPM detector was operated with a breakdown voltage $V_{\mathrm{breakdown}} = 24.7\,\mathrm{V}$ and an overvoltage $V_{\mathrm{OV}} = 2\,\mathrm{V}$. A neutral density filter with an optical density of $OD = 1.3$ covered the whole area of the SiPM detector. The global ASIC settings were set the same as used for the inter-pixel time calibration (see Section 3.5) and the applied thresholds were $t1 = 10$, $t2 = 5$, and $tE = 60$.

Expected results

The following section briefly describes the OH^+ system and the kinetic energy release E_{KER} channels accessible at 0 eV collision energy. After a storage time of $\sim$ 100 s, the

OH^+ ions are dominantly in their rovibrational ground state $X^3\Sigma^-$. The dissociation channels accessible at 0 eV collision energy are shown in Table 4.1, as presented in [35]. The corresponding expected kinetic energy releases with respect to the ground state can be calculated using

$$E_{KER} = IP(\mathrm{H}) - E_{\mathrm{O}_{state}} - D_0(\mathrm{OH}^+), \tag{4.1}$$

with the ionization potential of neutral Hydrogen $IP(\mathrm{H}) \sim 13.60$ eV [36], the energy of the accessible atomic Oxygen state $E_{\mathrm{O}_{state}}$ [36] (as in Table 4.1) and the dissociation energy of OH^+ $D_0(\mathrm{OH}^+) \sim 4.99$ eV [37]. It is to be noted that at 0 eV collision energy, no excited H fragments can be produced in dissociative recombination of OH^+.

Using Equation 2.4, the expected 3D distance D of a channel can be calculated with the respective kinetic energy release E_{KER}, the reduced mass of the ion, the ion beam velocity, and the distance from the interaction region to the detector. Since the ion beam energy E_0 is very high compared to the energy distribution of the ions produced in the source, the stored beam is assumed to be mono-energetic with a velocity v_0 along the beam direction (given by Equation 2.2). With a total ion mass of $M \sim 17\,\mathrm{u}$ for OH^+ and a typical value of $E_0 \sim 280\,\mathrm{keV}$, the velocity of the OH^+ ions is $v_0 \sim 178 \times 10^4\,\frac{\mathrm{m}}{\mathrm{s}}$. The distance from the electron-ion interaction region to the detector is $L \sim 3.8\,\mathrm{m}$. Since the interaction region in the electron cooler has a length of $\Delta L \sim 1\,\mathrm{m}$, the 3D distance of one channel is not a sharp value, but follows a distribution (box function). Maximum D_{max} or minimum 3D distance D_{min} of one channel assumes the position of dissociation to be at $L + (\Delta L/2)$ or $L - (\Delta L/2)$, respectively. The 3D distances for the channels accessible at 0 eV collision energy are displayed in Table 4.1.

Combined distance distribution

The 3D distance is also the squared sum of the transversal 2D distance d and the longitudinal distance $\Delta z = v_0 \Delta t$. It is practical to plot d vs Δz in a combined distance

Table 4.1: Accessible OH^+ DR channels at 0 eV collision energy. The table shows the final state of the reaction products and the kinetic energy release E_{KER} with respect to the rovibrational ground state of the OH^+-ion $X^3\Sigma^-$, as well as the mean 3D distance D and and the minimum D_{min} and maximum D_{max} possible 3D distances, which are a result of the electron cooler length.

O state	H state	E_{KER} (eV)	D (mm)	D_{min} (mm)	D_{max} (mm)
^{3}P	^{2}S	8.63	89.83	77.78	101.87
^{1}D	^{2}S	6.66	78.91	68.33	89.49
^{1}S	^{2}S	4.44	64.43	55.79	73.07

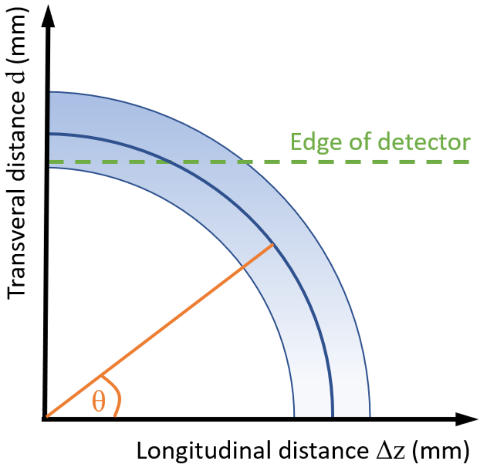

Figure 4.1: Schematic drawing of a combined distance distribution. The transversal 2D distance d is plotted against the longitudinal distance Δz of the impinging neutral fragments. The angle between the two axes corresponds to the dissociation angle θ. The dashed line marks a possible cut-off due to limited detection area of the MCP.

distribution, as shown in Figure 4.1 for one hypothetical kinetic energy release channel. There, the 3D distance is represented as the radial distance from the origin. The orientation of the molecular axis at the point of dissociation with respect to the ion beam axis, angle θ, is resolved as the angle between Δz and d. Due to the random orientation between the molecular axis and the electron impact vector at 0 eV, the process is symmetrical and we display the θ angle only in the $0° - 90°$ range.

As mentioned above, due to the length of the reaction zone, i.e. the electron cooler length, the distribution is not a sharp quarter of a circumference, but reflects the length of the reaction zone.

For large E_{KER}, it is possible that the distance between the two fragments will be too large, so that the lighter particle is not detected on the MCP. In this case, part of the 3D distance distribution is cut away for large 2D distances as displayed by the dashed green line in Figure 4.1. For OH^+ such cut-off is relevant for $E_{KER} \gtrsim 3.4$ eV, i.e. for all channels from Table 4.1.

4.2 Imaging performance

We tested the performance of the SiPM detector using the fragments from dissociative recombination of the diatomic molecular ion OH^+ as described in Section 4.1.

As an overview of the imaging capability Figure 4.2 shows the image of the bright light spots induced on the phosphor screen captured by both the CMOS camera (a) and the SiPM detector (b). On both images, the round shape of the MCP is clearly visible without noise events outside the detection area. As it will be discussed further below, the signal here originates dominantly from the DR fragmentation, i.e., neutral O and H fragments are detected. Due to the mass difference of the heavier oxygen atom and the light hydrogen atom, oxygen is detected close to the center of mass, i.e., the beam axis, with a distance of $3-6$ mm with respect to it, depending on the dissociation channel and the position in the interaction region at the time of dissociation. The enhanced intensity close to the detector center (at $\sim$ (275|250) pixel coordinate in the CMOS camera) is thus dominated by the O fragments and marks well the projected beam center. For the hydrogen atom this distance ranges between $\sim 53-96\,\mathrm{mm}$, with respect to the center-of-mass. In our case, the latter distance is too large to fit on the MCP ($d_{\mathrm{MCP}} = 120\,\mathrm{mm}$), since the beam is close to the center of it. This results in a cut off of the transverse distance distribution, as discussed in Section 4.1. On the left side of the circle is a region of less intensity, which is due to a laser mirror holder, which is in front of the MCP and shadows part of it.

4.2.1 Position correlation

Figure 4.3 shows the correlation in the position of the measured events with the CMOS camera (part of CSR-DAQ) against the SiPM detector, both in pixel. Only events with a single hit were considered in the plots, because multi-hit events are not sorted in the same way in both datasets. Figure 4.3 (a) displays the correlation for the x-axis and (b) one for the y-axis. One observes a linear relation between the position on the SiPM detector and the CMOS camera in both plots. This behavior is expected for a working synchronization between the two data acquisition systems CSR-DAQ and SiPM-DAQ. It is apparent, that for the y-axis the correlation is inverted, indicating that the image on the SiPM detector is flipped on the y-axis compared to the image on the CMOS camera. If needed this can easily be changed by changing the channel map, which refers to each channelID of the SiPM detector a pixel index, which can be found in Table B.1

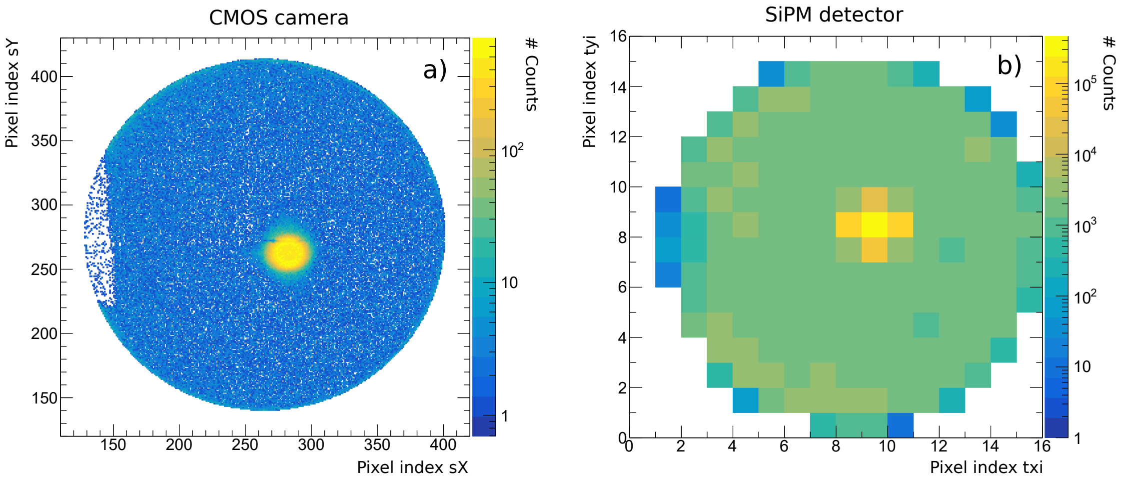

Figure 4.2: Image of the reaction products from DR of OH$^+$ ions on the fast CMOS camera (a) and the SiPM detector (b).

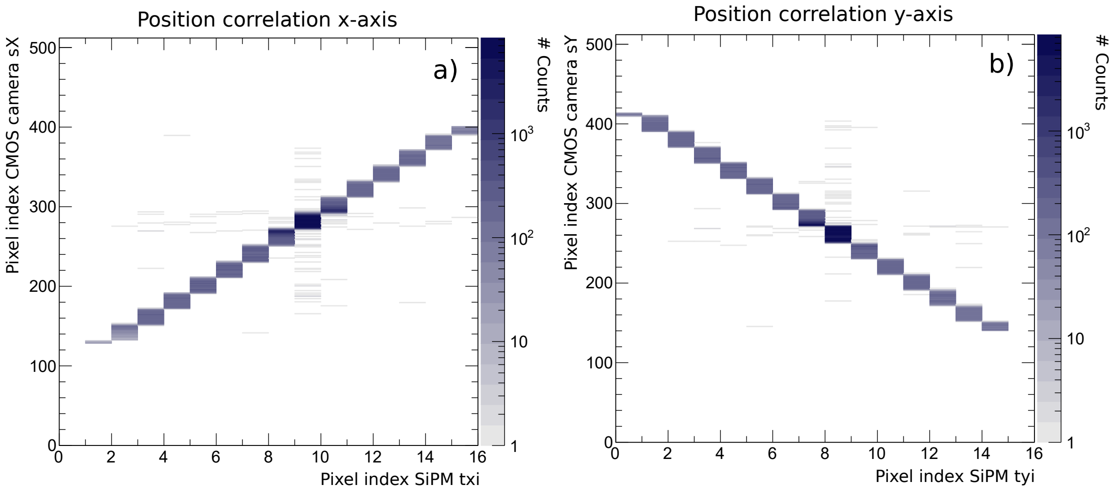

Figure 4.3: Position correlation of the SiPM- and CMOS camera events after synchronization. Panel (a) displays the correlation for the x-axis, while panel (b) shows the same for the y-axis. The number of counts is represented by the color-code.

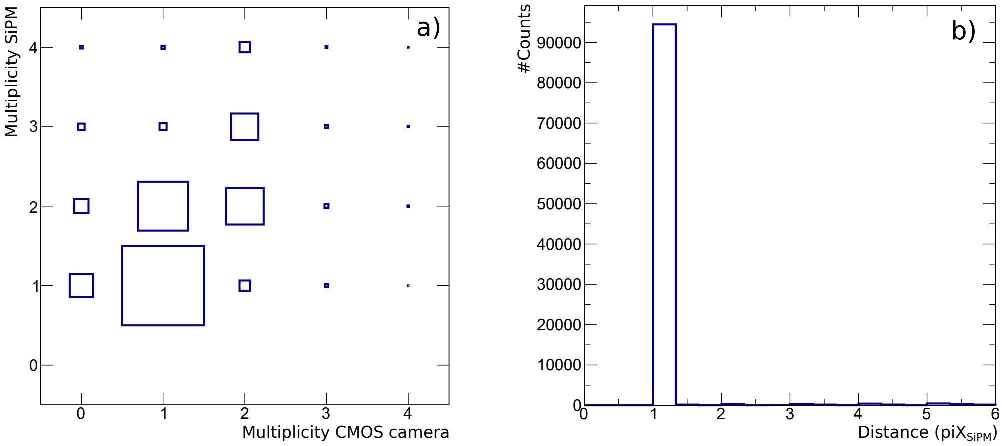

Figure 4.4: The multiplicity of the SiPM detector versus the multiplicity of events from the fast CMOS camera are shown in (a). The size of the boxes corresponds to the number of events in the respective configuration. Panel (b) displays the distance in SiPM-pixel for singles in the SiPM and for doubles in the CMOS camera.

in Appendix B.

The color-code of both plots shows the number of counts per pixel. The most hit pixel at the position $txi = 9$ and $tyi = 8$ in the SiPM plane marks the projected position of the ion beam center. In the vicinity of this pixel a cross-like feature is noticeable consisting of very few counts per pixel. This is probably due to random coincidences of unrelated events, where each of the detection system was unable to detect one of the impact due to dead-time effects. The fraction of such events is only $\sim 10^{-4}$.

All in all, the position correlation shows the expected linear behavior demonstrating, a good synchronization between the imaging readout of the fast CMOS camera and the SiPM detector.

4.2.2 Multiplicity

The multiplicity of an event gives the number of individual signals in said event. A *single* denotes an event with only one signal contributing in this event. If two signals are in one event, for example as is expected for the reaction products of dissociative recombination of diatomic molecular ions, it is referred to as *double*. In case three signals contribute to one event, it is described as *triple*. Here, we compare the multiplicities from the SiPM and the camera detection systems. In an ideal case the number of impact particles equals to the number of detected signals within an event, for both the SiPM detector and the CMOS camera.

Figure 4.4 (a) shows the multiplicity of the events measured with the SiPM detector tN against the multiplicity of events recorded with the fast CMOS camera sN. The boxes in the plot show the correlation between the multiplicity of both imaging readout options of the NICE detector. The size of the boxes corresponds to the number of events in the respective configuration, i.e., the configuration $sN = 1$ and $tN = 1$ represents the largest box.

For the physical impact events we expect mainly singles and doubles. The doubles are dominated by DR, singles by other physical processes like collisional dissociation on residual gas. DR can also contribute to singles, i.e., in the case when one fragment does not hit the detection area. Higher multiplicities are only expected from random coincidences. On the detector level, it is mainly the MCP detection efficiency of $\sim 60\,\%$ which can lower the detected multiplicity (i.e., DR is resolved as a single). This affects all three readouts of the NICE detector, the digitized anode signal, the CMOS camera, and the SiPM detector. The different nature of the various readouts can mix the detected multiplicities further, as discussed below.

In Figure 4.4 (a) we see that our setup does not exhibit linear behaviour. The largest fraction of events are both recorded as singles in the SiPM detector $tN = 1$ and the CMOS camera $sN = 1$. The second largest fraction of events are not doubles in both readout options, but singles in the CMOS camera $sN = 1$ and doubles in the SiPM readout $tN = 2$. The ratio between doubles and singles in the SiPM is about 38%, in case there are only singles in the CMOS camera. Moreover, the SiPM detects multiple signals when the CMOS camera detects none ($sN = 0$). This hints at a higher sensitivity of the SiPM detector compared to the CMOS camera.

The apparent higher multiplicity of the SiPM detector could also be due to the fact that neighboring SiPM pixels get triggered with a single impact. Figure 4.4 (b) shows the distance in pixels on the SiPM detector for events recorded as doubles on the SiPM but singles on the CMOS camera. The histogram clearly shows that mostly neighboring pixel respond in the SiPM detector. Figure 4.5 (a) displays the image of the phosphor screen on the CMOS camera of all events, where a single was recorded by the CMOS camera, but a double measured by the SiPM detector. A pattern of squares is clearly visible, with most of the events lying along the perimeter of the squares and delimiting them. The squares correspond to the pixel size of the SiPM detector. Therefore, the events delimiting the squares are single events on the CMOS camera but seen as doubles on the SIPM detector. This suggests that the spots from the phosphor screen have a non-zero size when projected on the SiPM plane. Spots imaged at the edge of a SiPM pixel trigger also the neighboring pixel. As expected, the pixel illuminated by the center

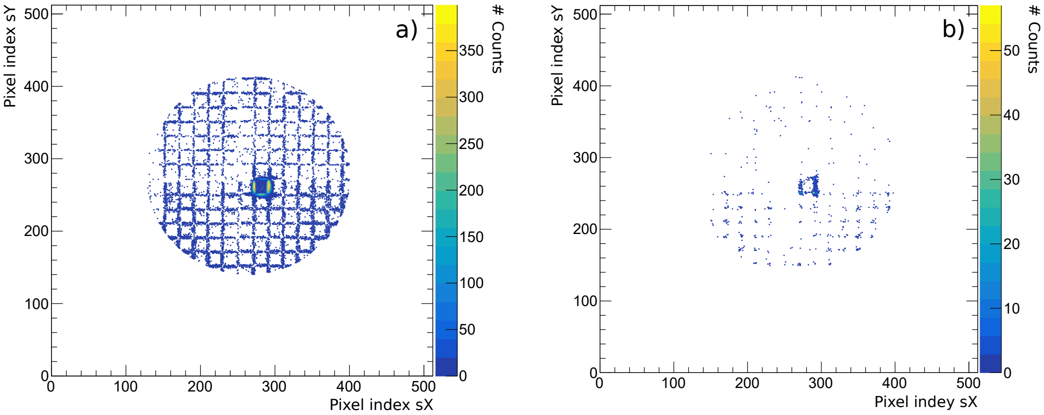

Figure 4.5: Image of single events in the CMOS camera, which are measured as doubles (a) or triplets (b) on the SiPM detector.

of the ion beam constitutes the square with the most events.

We also observe more events in the gaps between the squares in the lower half of the circle. This hints at a higher sensitivity of the upper two arrays of the SiPM detector connected to one FEM board (recalling the flipped position correlation between the SiPM detector and the CMOS camera on the y-axis).

The same is observed Figure 4.5 (b), which also displays the image on the CMOS camera for single events, but triplets in the SiPM detector. This shows us that the photons imaged on the corner of a gap between pixels on the SiPM detector can result in signals from three pixels of the SiPM detector, especially of the upper two arrays and in the central beam region, and supports the impression that the detector is set too sensitively. It also upholds the suspicion that the spot size on the SiPM plane is too large, so that a spot imaged on the edge of a SiPM pixel is able to trigger multiple pixels, since there is no intrinsic inter-pixel crosstalk in one SiPM array [38].

In the future the issue that one spot triggers multiple SiPM pixels can be improved by fine-tuning the threshold settings of the SiPM detector, adjusting the position of the focusing lens in front of the SiPM detector, or placing a neutral density filter with a higher optical density in front of the SiPM detector to reduce the photon flux.

4.3 Timing performance

As mention before, the goal of the newly implemented SiPM readout is to improve the time resolution for 3D-imaging. Therefore we compare the the timing behavior of the SiPM detector with the digitized anode signal of the MCP/Phosphor screen setup as

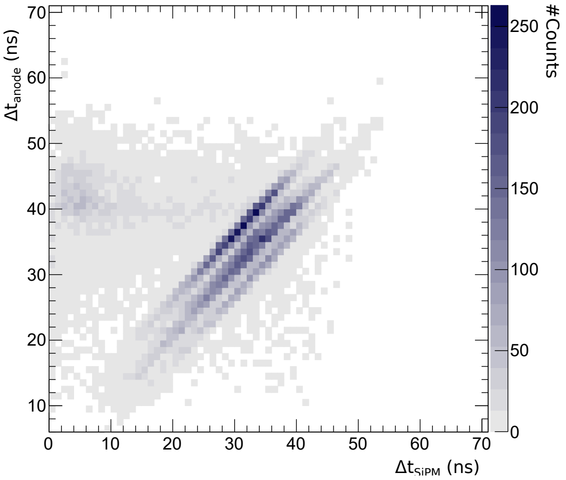

Figure 4.6: Correlation of the time difference between two signals in one event from the SiPM and digitized anode pulses. The color-code represents the number of counts.

used.

4.3.1 Time correlation

For calculating the 3D distance of two impinging molecular fragments, the time difference between those two is essential (see Equation 2.8) as it determines the longitudinal distance of the two fragments.

In Figure 4.6 the time difference of two signals of double events in the digitized anode signal ($\Delta t_{\mathrm{anode}}$) is plotted against the time difference of two signals of doubles in the SiPM detector (Δt_{SiPM}), both in ns. For this plot we expect a linear correlation between the two time differences, as they should essentially be the same. This is in principle what one can see in Figure 4.6. But two particular features are immediately noticeable: First, the linear trend consists of three lines close together, with a distance of about 5 ns. Second, there is a region at $30\,\mathrm{ns} < \Delta t_{\mathrm{anode}} < 55\,\mathrm{ns}$ where the anode times seem to have no correlation to the SiPM data. The latter point is discussed in detail in Section 4.3.2. For the three line issue we considered multiple hypotheses, e.g., possible instability of the pulse recognition algorithm on the anode signal, or relation to specific SiPM pixels. Till now, however, we could not confirm any of those hypotheses. However, from the more detailed discussion in Section 4.3.3 we assume that the timing issue is on the side of the SiPM readout.

4.3.2 Combined distance distribution

As mentioned above, we expect double hits for physical impact events from DR. Therefore, the 3D distance distribution is plotted only for double events in both the fast CMOS camera and the SiPM detector and is displayed in Figure 4.7. For a combined distance distribution plot, the transversal distance d is plotted against the longitudinal distance Δz of the two fragments, as explained in Section 4.1. Figure 4.7 (a) shows the combined distance distribution with Δz being based on the timing information of the digitized signal of the phosphor screen anode, while Figure 4.7 (b) shows the same, but uses the arrival times measured by the SiPM detector.

The transverse distance d is calculated using the positions of the two spots in an event measured by the CMOS camera and applying a pixel-to-mm calibration function. For that purpose a calibration mask, which is essentially a movable flap on the NICE detector, is put in front of the MCP. The mask has holes in a distance of 10 mm covering the area of the MCP, so that only particles passing through the holes can be projected on the detector, creating a pattern also visible by the CMOS camera. With this information a pixel-to-mm calibration can be performed. For the analyzed dataset we employed a simple linear fit which gives us the following calibration functions for the X- and Y-direction:

$$X[\text{mm}] = 0.4217 \times X[\text{pix}] \tag{4.2}$$

$$Y[\text{mm}] = 0.4401 \times Y[\text{pix}] \tag{4.3}$$

Using this pixel-to-mm calibration we determined the transversal 2D distance d of the fragments' position on the MCP as observed as bright light spots from the CMOS camera.

The longitudinal distance $\Delta z = v_0 \, \Delta t$ is determined using the ion beam velocity v_0 and the arrival time difference Δt of the two fragments.

As discussed in Section 4.1, the expected combined distance distribution progression follows the shape of quarter of a circle with width corresponding to the length of the interaction region in the experimental setup. Figure 4.1 displays a schematic drawing of an expected combined distance distribution.

Looking at Figure 4.7 (a), which shows the combined distance distribution using the arrival time difference of the fragments from the digitized signal of the phosphor screen anode Δz_{anode}, the expected behavior is visible. Immediately, the radius ($\sim$ 78 mm) and width ($\sim$ 25 mm) of the arc suggest that most OH$^+$ DR events result in H fragments in the ^2S ground state and O fragments in the ^1D excited state (see Table 4.1). Another thing that also attracts immediate attention is the cut off of events with a 2D distance

$d > 75\,\mathrm{mm}$. This is due to the finite size of the detector resulting in a banana-shaped distribution and not the expected quarter of a circle. It is to be noted that because of the non-centered ion beam projection on the detector (see Fig. 4.2) the cut off is not a sharp boundary. Another striking feature is the cut off in the longitudinal distance direction for $\Delta z_{\mathrm{anode}} < 16\,\mathrm{mm}$. For small longitudinal distances z, the induced pulses from the phosphor screen anode start to overlap. At some point the digitizer is not able to resolve them anymore. This issue is a limiting factor for the 3D-imaging resolution of the NICE detector using the timing information of the fragments from the digitized phosphor screen anode signal. With the implemented SiPM readout option we aim to solve this issue.

In Figure 4.7 (b) the combined distance distribution is displayed using the timing information of the SiPM detector to calculate the longitudinal distance Δz_{SiPM}. Compared to Figure 4.7 (a) more events over the inner area of the circle are visible. The cut on fragments with a large transverse distance $d > 74\,\mathrm{mm}$ is again clearly visible. A striking detail of this plot is a distortion of the distribution for small transversal distances $d < 20\,\mathrm{mm}$ with a high intensity feature for small longitudinal distances $\Delta z_{\mathrm{SiPM}} < 25\,\mathrm{mm}$. We assume that the high intensity feature was shifted from the circular shape for large longitudinal and short transversal distances. For small transverse distances, the SiPM seems to be unable to resolve the time information properly. Since the time difference of the two signals are small compared to the anticipated large time differences at short transversal distances, it could be possible that the time stamp of the latter signal is wrongly assigned. We think that signal pile-up is the origin of this issue, since the first impact can also induce a small signal on the neighbouring SiPM pixels. While such signal is too low to trigger full detection, it can overcome the low threshold for determining the impact time. The second impact then brings the signal over the full-detection threshold, but the time is taken from the small parasitic signal from the first impact. Therefore, the time stamp of the hit is too early with respect to the first hit in the event.

4.3.3 Timing precision test

Applying cuts on the dissociation angle θ gives insight in the time precision af the detection system. The 3D distance distribution at $0\,\mathrm{eV}$ collision energy should not depend on the angel θ due to the randomized collision orientations. In case detector effects are present, cuts in θ can emphasize them, e.g., applying a cut close to $\theta = 0$ will emphasize the contribution from the detector time readout (anode signal or SiPM), while a cut close to $\theta = \pi/2$ would emphasize the transverse position detection using

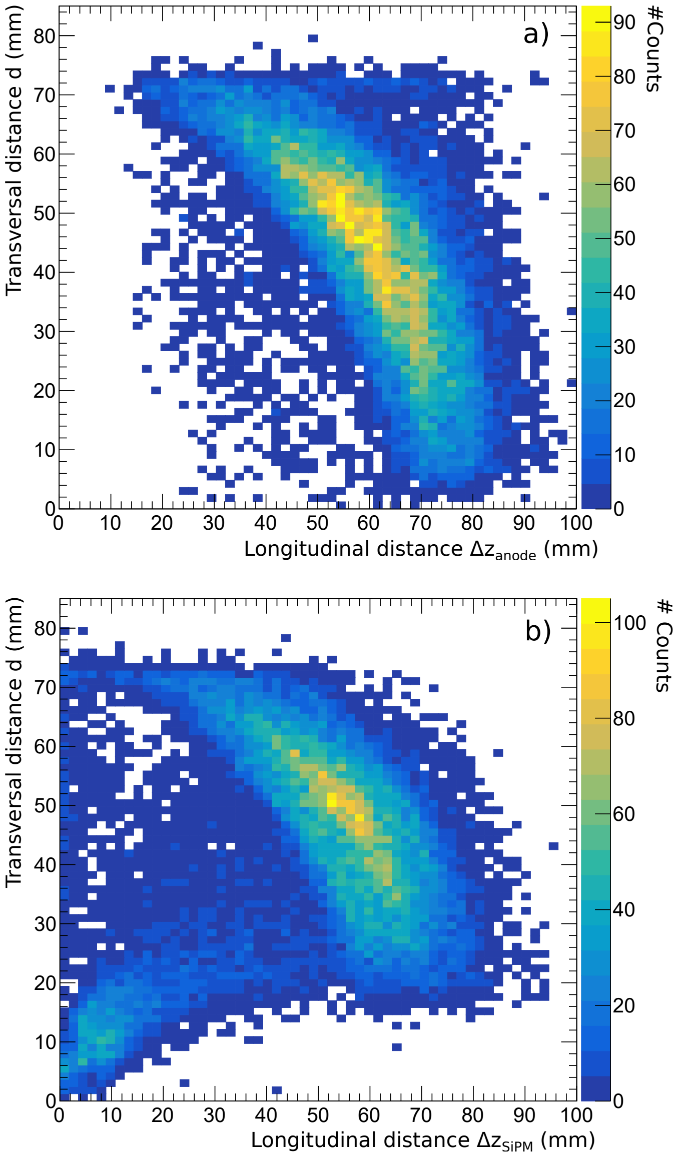

Figure 4.7: Combined distance distribution of two signals in one event-double. The transverse distance of the two particles in one event d, derived from the impact position information measured with the fast CMOS camera, is plotted against the longitudinal distance Δz of the two fragments. Plot (a) uses the digitized anode signal of the MCP/Phosphor screen setup to derive Δz. Plot (b) uses the timing information recorded with the SiPM readout. The z-axis displays the number of counts in both plots.

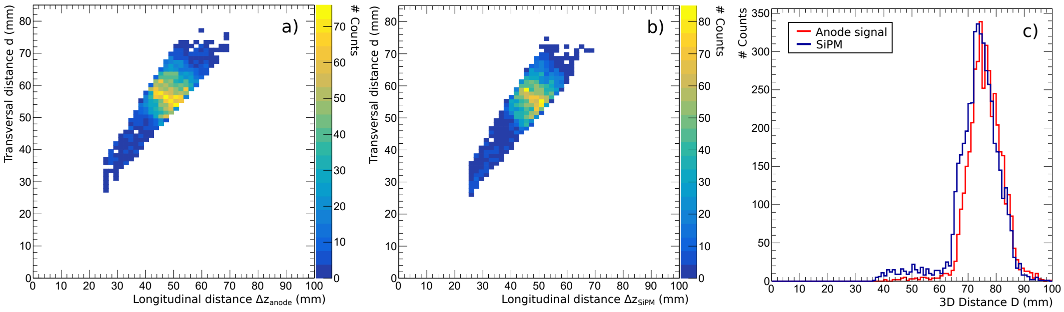

Figure 4.8: 3D distance for large angular cuts. Panels (a) and (b) show the combined distance distribution for large dissociation angles ($0.80 < \theta < 0.95$) using the timing information of the anode signal and the SiPM detector, respectively. Panel (c) displays the 3D distance distribution for said events. The red histogram corresponds to the data employing anode-signal timing and the blue one to the SiPM detector.

the CMOS camera. Unfortunately, the limitations of the various readout systems, e.g., detector size, as discussed above, additionally distort the 3D distance distribution and not as extreme angular cuts like $\theta = 0$ and $\theta = \pi/2$ could be applied on our data. Still, we were able to find angular ranges preferring the timing and position contribution. For small angles a cut ranging between $0.35 < \theta < 0.50$ was applied, and for large angles a cut ranging between $0.80 < \theta < 0.95$, respectively.

Figure 4.8 shows the 3D distance D for dissociation angles between $0.80 < \theta < 0.95$. To further minimize the contribution of detection artefacts, events with a 2D distance $d < 20\,\mathrm{mm}$ and a longitudinal distance $\Delta z < 25\,\mathrm{mm}$ were omitted. Panels (a) and (b) of Figure 4.8 display the allocation of the events in the combined distance distribution (as in Figure 4.7) employing the above described cut for the anode signal time and the SiPM time, respectively. Panel (c) shows the 3D distances for said events. The red histogram gives the 3D distance distribution using the anode signal time and the blue histogram using the SiPM time. It can be observed, that both histograms have a similar shape peaking around $D \sim 74\,\mathrm{mm}$. Events with a 3D distance $D < 65\,\mathrm{mm}$ can be denoted as noise effects, the fraction being higher in the SiPM histogram than in the anode signal histogram. Physical 3D distances range from $D \sim 60\,\mathrm{mm}$ to $D \sim 90\,\mathrm{mm}$. Comparing these values with Table 4.1, we can infer the dissociation channels with the product states $\mathrm{O}(^1\mathrm{D}) + \mathrm{H}(^2\mathrm{S})$. It appears that the SiPM histogram is shifted $\sim 1\,\mathrm{mm}$ to shorter 3D distances compared to the signal anode histogram.

In Figure 4.9 the 3D distance distribution is shown in the same way as in Figure 4.8, but for small dissociation angles between $0.35 < \theta < 0.50$. The 3D distance between the

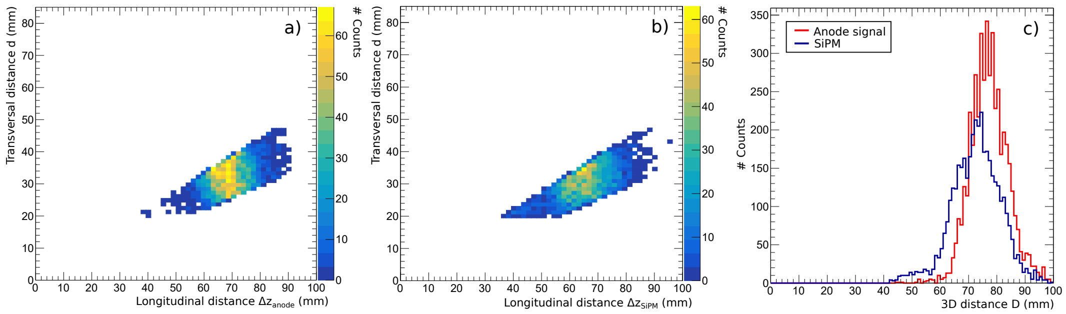

Figure 4.9: 3D distance for small angular cuts. Panels (a) and (b) show the combined distance distribution for small dissociation angles ($0.35 < \theta < 0.50$) using the timing information of the anode signal and the SiPM detector, respectively. Panel (c) displays the 3D distance distribution for said events. The red histogram corresponds to the data employing anode signal timing and the blue one to the SiPM detector.

SiPM data (blue) and the data acquired with the anode signal (red) differs a lot – much more than in Figure 4.8 for large dissociation angles, hinting that one detection system has a varying time precision. Figure 4.10 illustrates this further. Each panel shows the 3D distances for one detection system, comparing the time precision for large (red) and small (blue) dissociation angles θ for the anode timing (a) and the SiPM timing (b). For the 3D distances with timing information acquired with the anode signal no clear difference is recognizable, suggesting that the precision of the transverse and longitudinal data is comparable. Contrary to this Figure 4.10 (b) displays a distinct difference of the time precision for the SiPM detector. For small angles, where the timing information dominates the 3D distribution, the precision is worse than for larger angles. Clearly, the longitudinal distances derived from the SiPM timing are distorted in the test data. The 3D distribution for the SiPM at small θ angles, which is dominated by the timing information, is broader (by $\sim$ 16%) and shifted to smaller Δz_{SiPM} (by $\sim$ 3%) when compared to the distribution of the anode signal timing data. This may be partly due to signal pile-ups as well as a too low set threshold for determining the SiPM event-time, which can lead to overlapping pulse shapes.

4.3.4 Timing resolution test

As discussed above, the main reason for implementing the SiPM array readout of the NICE detector is its intrinsic ability to resolve the impacts independently of the impinging fragments' time difference. This holds well for cases where the detected spots from the individual impacts do not overlap in the SiPM pixels. In Section 4.3.2 it was

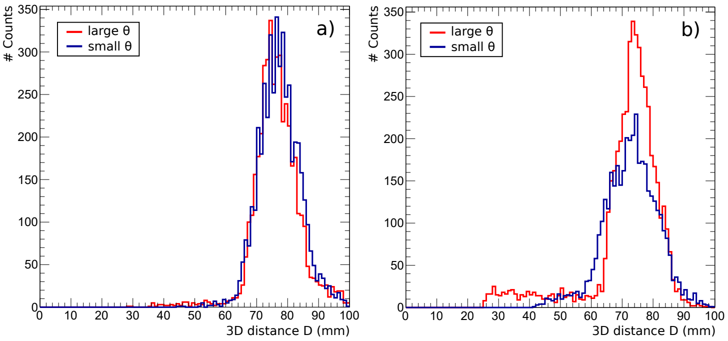

Figure 4.10: 3D distance distributions for large (red) and small (blue) dissociation angles. Panel (a) compares the time precision for the anode signal and panel (b) for the SiPM detector.

shown that such limitation occurs for spot-distances $\lesssim 2$ pixels in the SiPM. However, for larger distances the timing of the individual impacts is well resolved, even though the current setting results in a timing precision somewhat worse when compared to the anode signal timing readout.

For demonstrating the detectors ability to resolve impact time differences down to zero we concentrate on detected events where the two DR fragments are oriented at $\theta \sim \pi/2$, i.e., they hit the detector at a large transverse distance, but simultaneously. Unfortunately, in such cases the high E_{KER} of OH^+ DR results in too large transverse distances and most such events cannot be detected for geometrical reasons. Still, in Figure 4.7 (b) one can see a clear enhancement of SiPM-detected events at very small longitudinal distances (see transversal distance $d \gtrsim 70\,\mathrm{mm}$) when compared to the data using the anode signal timing (Figure 4.7 (a)). To emphasize this effect further, we concentrate on DR-induced events resolved by the SiPM (doubles), but non-resolved by the anode-signal readout by the digitizer (singles), i.e., on the events where the SiPM resolution outperforms that of the anode-signal readout. The so filtered events are plotted in Figure 4.11 as the combined distance distribution. Also here, the data enhancement at $d \gtrsim 70\,\mathrm{mm}$ follows the expected shape for the OH^+ DR and reaches longitudinal distances down to $\Delta z = 0$, thus proving the SiPM resolution qualities. The data at $\Delta z \gtrsim 30$ mm show the overall higher sensitivity of the SiPM readout compared to the anode signal digitization.

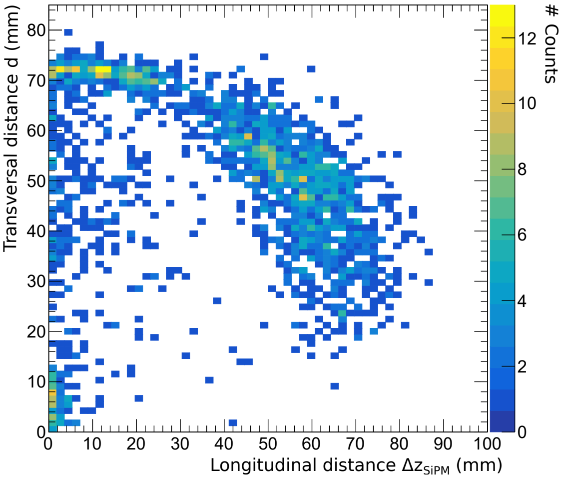

Figure 4.11: Combined distance distribution filtered on doubles detected with the SiPM, but singles in the digitized phosphor screen anode signal. Pulses that are not resolved by the digitizer can be resolved using the SiPM readout.

4.4 Discussion

The acquired data reveals the complex behavior of the SiPM detector, which in some cases affects sub-optimally its performance, or complicates the data interpretation. However, most of the behavior is understood and we propose approaches for improving the SiPM performance in the future.

First, we observe an increased multiplicity in the SiPM detector compared to the CMOS camera (Figure 4.4 (a)). A cause for this is the macroscopic spot size from the phosphor screen projected on the SiPM plane. This is also supported by the fact, that for events recorded as singles in the CMOS camera, but doubles in the SiPM, mostly neighboring SiPM-pixels are hit (Figure 4.4 (b)). Also measured doubles and triples in the SiPM are found to be close to the boundary between the SiPM pixels (Figure 4.5). Using the high-resolution CMOS camera we estimate, that the spots on the phosphor screen project to the SiPM detector plane at a diameter of $\lesssim 0.8\,\mathrm{mm}$. Thus, given the $0.36\,\mathrm{mm}$ gaps between the SiPM pixels, the enhanced multiplicity on SiPM due to spots covering neighboring pixels is plausible. Reducing the spot size, e.g., by better focusing, may lower the multiplicity enhancement. But on the other hand too small spots could be projected solely in the insensitive gap between the SiPM pixels and the overall detection sensitivity would drop. It may be more easy to combine the imaging capability of the CMOS camera and the SiPM array to identify the critical cases and treat them on the software side, e.g., by identifying the triggered neighboring SiPM pixels as one impact.

Apart from this, in Figure 4.5 (a) we see that the lower half (the image is flipped on the y-axis) of the SiPM detector records less events compared to the upper half. The observed sensitivity difference between the upper and lower half of the SiPM detector could be corrected by increasing the overvoltage for the lower two arrays, which would result in a higher gain.

Moreover, we realize that the timing information of multi-hit events in the SiPM is incorrect for small transversal distances between the impacting particles of $\lesssim 2$ SiPM-pixels (seen in Figure 4.7 (b) and Figure 4.10 (b)). A reason for this could be a signal pile-up. A first impact induces also a small signal in a neighboring pixel, overcoming the first low timing threshold. The second impact then brings the signal over then full-detection threshold, but keeps the timing from the parasitic signal of the first impact. Initially, we set the first timing threshold intentionally low, for a more accurate impact time measurement, independent of the pulse height. Alternatively, the threshold can be set higher to avoid triggering on the parasitic signals, and the trigger-time can be corrected to determine the precise impact time, using the known pulse shape and measured pulse height.

The precision on the impact times is at an acceptable level for resolving the DR channels in the case of OH^+, although we have shown that it is not as good as the timing from the anode signal readout. Also here further tests are needed to optimize the timing quality in dependency on the various thresholds, a procedure which could not have been completed within the scope of this thesis. On the positive side, the main goal of the detector upgrade with the SiPM array was fulfilled: the impact times can be resolved for independent impacts down to zero time difference, with the limitation on the minimum transverse impact distance of $\gtrsim 2$ SiPM-pixel. For future applications the timing readouts from the anode signal and SiPM can be combined so that the combined limitations are minimized. It is expected that Monte-Carlo simulations of the detector behavior, similar to that for the EMU detector at the TSR storage ring [39], will help to take into account the various aspects of the three NICE detector readout branches.

5 Summary and Outlook

In the scope of this thesis a new setup for an additional timing readout of the molecular fragment imaging detector NICE at the Cryogenic Storage Ring CSR in Heidelberg was designed, commissioned and tested. A new timing readout was necessary to improve the time resolution of the detector. The previously implemented time readout uses a digitized signal of the non-segmented phosphor screen anode. The limiting factor hereby is that pulses generated by particles impacting close in time ($\Delta t \lesssim 15\,\mathrm{ns}$) overlap and can not be resolved. A segmented readout option was proposed and implemented within this work to improve on this issue.

For this purpose a new optical readout setup was designed, constructed and commissioned to include a SiPM detector, consisting of 16×16 pixels, in the pre-existing NICE detector setup. This included the construction of a new optical table and holder for the SiPM detector and its readout electronics, as well as the configuration and the testing of the SiPM detector, and the search for optimal operational settings. Moreover, the data acquisition systems of the SiPM had to be tested and synchronized with the main CSR-DAQ system to combine the information measured with the various readout options of the NICE detector.

The performance of the additional timing readout was tested during the OH^+ dissociative recombination beamtime in February 2021 and shows promising results. The acquired SiPM data was compared with the data acquired using the CSR-DAQ system. For the imaging performance the SiPM data was compared with the measured data from the CMOS camera, and for comparison of the timing information the pulses from the digitized anode signal were used. Here, specific behavior of the SiPM detector was observed. On the imaging side it is realized, that the multiplicity of the events acquired by the SiPM is in general higher than the one by the CMOS camera. This is due to a higher sensitivity of the SiPM and due to a non-zero size of the phosphor screen spots when projected on the SiPM data. The acquired data shows, that events recorded as doubles in the SiPM, but observed as singles in the CMOS camera, are mostly acquired by neighboring pixel. The data also demonstrates that such doubles in the SiPM detector mostly hit close to the edge of a SiPM pixel.

On the timing side, peculiar behavior for hits spatially close to each other is observed in the SiPM. This is likely due to a signal pile-up from combined signals of neighboring pixels resulting in a wrong timing for the later impact. It can be improved by adjusting the thresholds accordingly, i.e., rising the timing threshold.

Despite this specific behavior, the data reveals that the SiPM detector is able to resolve spatially well separated spots with impact time differences down to zero, which cannot be resolved by the anode signal. This shows that the SiPM setup fulfills the initial goal of the detector upgrade.

In the future the SiPM detector behavior has to be further investigated. For the reduction of the observed multiplicity in the SiPM, the spots from the phosphor screen projected on the SiPM plane can be reduced by varying the position of the focusing lens in front of the SiPM detector. But one has to keep in mind not to downsize the spots below the width of the insensitive gaps between the pixels, so that the overall detection efficiency would not be lowered. Applying a correction on the software side, e.g. by identifying the triggered neighboring pixels as one impact, could be an easier and more efficient solution.

A reduction in sensitivity of the SiPM detector can also improve the overall performance. To realize this, a neutral density filter with a higher optical density as the already employed one can be implemented. Further, optimizing the threshold setting will lower the sensitivity of the detector as well. Applying new threshold settings, especially for the timing thresholds, will help with the premature timestamping of impacts spatially close together. Since this behavior only applies to consecutive impacts with a spatial distance of $\lesssim 2$ pixel in the SiPM domain, the detector readouts can be combined in the future, which will be especially needed for multi-body fragmentation processes, like DR of H_3^+ into three hydrogen atoms.

Nevertheless, for further tests of the SiPM detector, it would be helpful to measure with a more suitable molecular ion, like CH^+, where no geometrical cut off is expected for the observed C+H fragmentation channels with $E_{KER} \lesssim 4.5\,\mathrm{eV}$.

Even though the SiPM will still be fine-tuned, its performance already now allows to well assign the product states of the dissociative recombination of OH^+ as acquired in the detectors' first-light beamtime in February 2021.

Part I

Appendix

A Lists

A.1 List of Figures

A.2 List of Tables

B Channel Map

Parameters of the four SiPM arrays as they are identified by the readout electronics from PETsys and the corresponding assigned coordinates for each pixel to create a channel map, in which each channel is assigned a (x|y) value.

portID: DAQ portID where the FEB/D board is connected.

slaveID: Identifies a FEB/D when connecting multiple FEB/Ds in daisy chain.

chipID: ID of the ASIC. Depends on where it is connected to the FEB/D board. If a FEM board is connected to port F1 on the FEB/D the chipID equals 0 and 1 for the two ASICs. For port F2 it the chipID is 2 and 3, and so on.

$channelID_{ASIC}$*:* ChannelID inside the ASIC, ranging from 0 to 63. With the help of table 6 – 8 of the "TOFPET2 ASIC SIPM Readout System - Hardware User Guide (v1.6)" [32] one can trace which pixel of a SiPM array is connected to its corresponding ASIC channel. It should be noted that we have the Ball-Grid-Version (BGA) of the ASIC board.

After the raw data processing, the software associates each ASIC channel, and therefore each pixel, an absolute channelID identifying each channel individually:

$$channelID = 131072 \times portID + 4096 \times slaveID + 64 \times chipID + channelID_{ASIC} \quad \text{(B.1)}$$

Since we only have one FEB/D board, and therefore do not need a DAQ card, the portID and the slaveID always equal zero.

The above described parameters are used to create a channel map. Table B.1 shows the channel map as we implemented it in the SiPM acquisition script as a tab separated text file. Additional parameters, that are not discussed above, are the regionID, the pixel index x_i and y_i, and the pixel's spatial position in x, y and$z$.

Channels with the same trigger regionID are grouped in one geometrical regions if the user enables the processing of coincident or multi-hit events in the PETsys data processing script. The software will for example only consider events as coincidence if they occur in different trigger regions. Since we did not use that option, the default values were kept in the table.

The pixel index numbers x_i and y_i are indices tagged to the event data. In the output ROOT-file they are implemented as a separate branch for each index and can be used to create a pixel map as for example shown in Figure 3.8. We verified the position of the pixels by illuminating them separately using the calibration mask with attached LED holder (Figure 3.6 (b)). Figure B.1 shows how the x_i and y_i from 0 to 15 were assigned to the pixels.

The spatial positions in $x-$, $y-$ and $z-$ direction in mm are given by the parameters with the same names. They are also used to group events by the data processing scripts provided by PETsys. Since we did not use them, the columns are kept empty.

The last column does not exist in the text file. It is only shown here to better clarify which pixel corresponds to which row.

A detailed description can be found in the PETsys TOFPET2 ASIC SiPM Readout System Software user guide v2019.09 p. 41 [40].

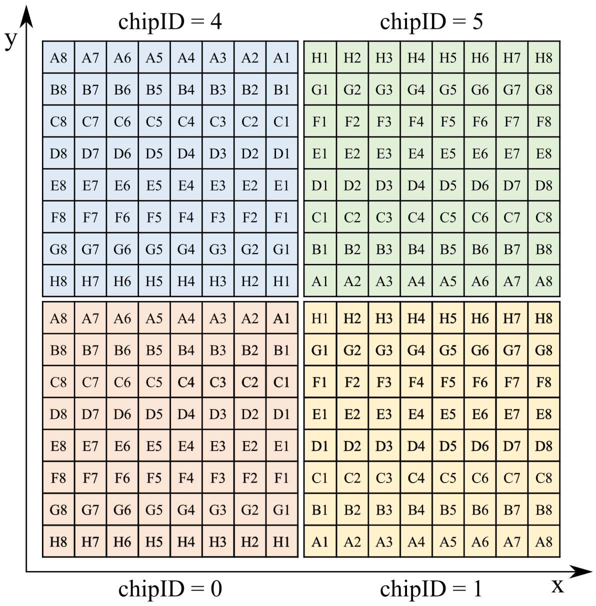

A8	A7	A6	A5	A4	A3	A2	A1	H1	H2	H3	H4	H5	H6	H7	H8
B8	B7	B6	B5	B4	B3	B2	B1	G1	G2	G3	G4	G5	G6	G7	G8
C8	C7	C6	C5	C4	C3	C2	C1	F1	F2	F3	F4	F5	F6	F7	F8
D8	D7	D6	D5	D4	D3	D2	D1	E1	E2	E3	E4	E5	E6	E7	E8
E8	E7	E6	E5	E4	E3	E2	E1	D1	D2	D3	D4	D5	D6	D7	D8
F8	F7	F6	F5	F4	F3	F2	F1	C1	C2	C3	C4	C5	C6	C7	C8
G8	G7	G6	G5	G4	G3	G2	G1	B1	B2	B3	B4	B5	B6	B7	B8
H8	H7	H6	H5	H4	H3	H2	H1	A1	A2	A3	A4	A5	A6	A7	A8
A8	A7	A6	A5	A4	A3	A2	A1	H1	H2	H3	H4	H5	H6	H7	H8
B8	B7	B6	B5	B4	B3	B2	B1	G1	G2	G3	G4	G5	G6	G7	G8
C8	C7	C6	C5	C4	C3	C2	C1	F1	F2	F3	F4	F5	F6	F7	F8
D8	D7	D6	D5	D4	D3	D2	D1	E1	E2	E3	E4	E5	E6	E7	E8
E8	E7	E6	E5	E4	E3	E2	E1	D1	D2	D3	D4	D5	D6	D7	D8
F8	F7	F6	F5	F4	F3	F2	F1	C1	C2	C3	C4	C5	C6	C7	C8
G8	G7	G6	G5	G4	G3	G2	G1	B1	B2	B3	B4	B5	B6	B7	B8
H8	H7	H6	H5	H4	H3	H2	H1	A1	A2	A3	A4	A5	A6	A7	A8

Figure B.1: Arrangement of the four KETEK PA3325 WB 0808 SiPM arrays in front view. Each pixel of one array is labeled by a letter and number arranged like in a matrix. The labelling was adopted from the datasheet [17]. If one looks at the SiPM detector from the direction of the photons, the lowest left pixel is labeled H8 with chipID = 0.

Table B.1: Parameters of the four SiPM arrays as they are identified by the readout electronics from PETsys and the corresponding assigned coordinates for each pixel to create a channel map, in which each channel is assigned to an (x|y) value. A detailed description of the parameters con be found in the text above.

portID	slaveID	chipID	channelID$_{\mathrm{ASIC}}$	regionID	xi	yi	x	y	z	Pixel
0	0	0	17	0	0	0	0	0	0	H8
0	0	0	18	0	1	0	0	0	0	H7
0	0	0	23	0	2	0	0	0	0	H6
0	0	0	20	0	3	0	0	0	0	H5
0	0	0	5	0	4	0	0	0	0	H4
0	0	0	14	0	5	0	0	0	0	H3
0	0	0	0	0	6	0	0	0	0	H2
0	0	0	10	0	7	0	0	0	0	H1
0	0	0	19	0	0	1	0	0	0	G8
0	0	0	16	0	1	1	0	0	0	G7
0	0	0	22	0	2	1	0	0	0	G6
0	0	0	21	0	3	1	0	0	0	G5
0	0	0	12	0	4	1	0	0	0	G4
0	0	0	7	0	5	1	0	0	0	G3
0	0	0	1	0	6	1	0	0	0	G2
0	0	0	3	0	7	1	0	0	0	G1
0	0	0	25	0	0	2	0	0	0	F8
0	0	0	28	0	1	2	0	0	0	F7
0	0	0	29	0	2	2	0	0	0	F6
0	0	0	32	0	3	2	0	0	0	F5
0	0	0	27	0	4	2	0	0	0	F4
0	0	0	13	0	5	2	0	0	0	F3
0	0	0	8	0	6	2	0	0	0	F2
0	0	0	4	0	7	2	0	0	0	F1
0	0	0	24	0	0	3	0	0	0	E8
0	0	0	26	0	1	3	0	0	0	E7
0	0	0	30	0	2	3	0	0	0	E6
0	0	0	31	0	3	3	0	0	0	E5
0	0	0	11	0	4	3	0	0	0	E4

0	0	0	2	0	5	3	0	0	0	E3
0	0	0	15	0	6	3	0	0	0	E2
0	0	0	6	0	7	3	0	0	0	E1
0	0	0	41	0	0	4	0	0	0	D8
0	0	0	39	0	1	4	0	0	0	D7
0	0	0	36	0	2	4	0	0	0	D6
0	0	0	33	0	3	4	0	0	0	D5
0	0	0	9	0	4	4	0	0	0	D4
0	0	0	62	0	5	4	0	0	0	D3
0	0	0	59	0	6	4	0	0	0	D2
0	0	0	50	0	7	4	0	0	0	D1
0	0	0	40	0	0	5	0	0	0	C8
0	0	0	37	0	1	5	0	0	0	C7
0	0	0	35	0	2	5	0	0	0	C6
0	0	0	34	0	3	5	0	0	0	C5
0	0	0	38	0	4	5	0	0	0	C4
0	0	0	58	0	5	5	0	0	0	C3
0	0	0	61	0	6	5	0	0	0	C2
0	0	0	57	0	7	5	0	0	0	C1
0	0	0	49	0	0	6	0	0	0	B8
0	0	0	45	0	1	6	0	0	0	B7
0	0	0	46	0	2	6	0	0	0	B6
0	0	0	43	0	3	6	0	0	0	B5
0	0	0	52	0	4	6	0	0	0	B4
0	0	0	53	0	5	6	0	0	0	B3
0	0	0	56	0	6	6	0	0	0	B2
0	0	0	63	0	7	6	0	0	0	B1
0	0	0	48	0	0	7	0	0	0	A8
0	0	0	47	0	1	7	0	0	0	A7
0	0	0	44	0	2	7	0	0	0	A6
0	0	0	42	0	3	7	0	0	0	A5
0	0	0	51	0	4	7	0	0	0	A4
0	0	0	54	0	5	7	0	0	0	A3
0	0	0	55	0	6	7	0	0	0	A2
0	0	0	60	0	7	7	0	0	0	A1

0	0	1	60	0	8	0	0	0	0	A1
0	0	1	55	0	9	0	0	0	0	A2
0	0	1	54	0	10	0	0	0	0	A3
0	0	1	51	0	11	0	0	0	0	A4
0	0	1	42	0	12	0	0	0	0	A5
0	0	1	44	0	13	0	0	0	0	A6
0	0	1	47	0	14	0	0	0	0	A7
0	0	1	48	0	15	0	0	0	0	A8
0	0	1	63	0	8	1	0	0	0	B1
0	0	1	56	0	9	1	0	0	0	B2
0	0	1	53	0	10	1	0	0	0	B3
0	0	1	52	0	11	1	0	0	0	B4
0	0	1	43	0	12	1	0	0	0	B5
0	0	1	46	0	13	1	0	0	0	B6
0	0	1	45	0	14	1	0	0	0	B7
0	0	1	49	0	15	1	0	0	0	B8
0	0	1	57	0	8	2	0	0	0	C1
0	0	1	61	0	9	2	0	0	0	C2
0	0	1	58	0	10	2	0	0	0	C3
0	0	1	38	0	11	2	0	0	0	C4
0	0	1	34	0	12	2	0	0	0	C5
0	0	1	35	0	13	2	0	0	0	C6
0	0	1	37	0	14	2	0	0	0	C7
0	0	1	40	0	15	2	0	0	0	C8
0	0	1	50	0	8	3	0	0	0	D1
0	0	1	59	0	9	3	0	0	0	D2
0	0	1	62	0	10	3	0	0	0	D3
0	0	1	9	0	11	3	0	0	0	D4
0	0	1	33	0	12	3	0	0	0	D5
0	0	1	36	0	13	3	0	0	0	D6
0	0	1	39	0	14	3	0	0	0	D7
0	0	1	41	0	15	3	0	0	0	D8
0	0	1	6	0	8	4	0	0	0	E1
0	0	1	15	0	9	4	0	0	0	E2

0	0	1	2	0	10	4	0	0	0	E3
0	0	1	11	0	11	4	0	0	0	E4
0	0	1	31	0	12	4	0	0	0	E5
0	0	1	30	0	13	4	0	0	0	E6
0	0	1	26	0	14	4	0	0	0	E7
0	0	1	24	0	15	4	0	0	0	E8
0	0	1	4	0	8	5	0	0	0	F1
0	0	1	8	0	9	5	0	0	0	F2
0	0	1	13	0	10	5	0	0	0	F3
0	0	1	27	0	11	5	0	0	0	F4
0	0	1	32	0	12	5	0	0	0	F5
0	0	1	29	0	13	5	0	0	0	F6
0	0	1	28	0	14	5	0	0	0	F7
0	0	1	25	0	15	5	0	0	0	F8
0	0	1	3	0	8	6	0	0	0	G1
0	0	1	1	0	9	6	0	0	0	G2
0	0	1	7	0	10	6	0	0	0	G3
0	0	1	12	0	11	6	0	0	0	G4
0	0	1	21	0	12	6	0	0	0	G5
0	0	1	22	0	13	6	0	0	0	G6
0	0	1	16	0	14	6	0	0	0	G7
0	0	1	19	0	15	6	0	0	0	G8
0	0	1	10	0	8	7	0	0	0	H1
0	0	1	0	0	9	7	0	0	0	H2
0	0	1	14	0	10	7	0	0	0	H3
0	0	1	5	0	11	7	0	0	0	H4
0	0	1	20	0	12	7	0	0	0	H5
0	0	1	23	0	13	7	0	0	0	H6
0	0	1	18	0	14	7	0	0	0	H7
0	0	1	17	0	15	7	0	0	0	H8
0	0	4	17	1	0	8	0	0	0	H8
0	0	4	18	1	1	8	0	0	0	H7
0	0	4	23	1	2	8	0	0	0	H6
0	0	4	20	1	3	8	0	0	0	H5
0	0	4	5	1	4	8	0	0	0	H4

0	0	4	14	1	5	8	0	0	0	H3
0	0	4	0	1	6	8	0	0	0	H2
0	0	4	10	1	7	8	0	0	0	H1
0	0	4	19	1	0	9	0	0	0	G8
0	0	4	16	1	1	9	0	0	0	G7
0	0	4	22	1	2	9	0	0	0	G6
0	0	4	21	1	3	9	0	0	0	G5
0	0	4	12	1	4	9	0	0	0	G4
0	0	4	7	1	5	9	0	0	0	G3
0	0	4	1	1	6	9	0	0	0	G2
0	0	4	3	1	7	9	0	0	0	G1
0	0	4	25	1	0	10	0	0	0	F8
0	0	4	28	1	1	10	0	0	0	F7
0	0	4	29	1	2	10	0	0	0	F6
0	0	4	32	1	3	10	0	0	0	F5
0	0	4	27	1	4	10	0	0	0	F4
0	0	4	13	1	5	10	0	0	0	F3
0	0	4	8	1	6	10	0	0	0	F2
0	0	4	4	1	7	10	0	0	0	F1
0	0	4	24	1	0	11	0	0	0	E8
0	0	4	26	1	1	11	0	0	0	E7
0	0	4	30	1	2	11	0	0	0	E6
0	0	4	31	1	3	11	0	0	0	E5
0	0	4	11	1	4	11	0	0	0	E4
0	0	4	2	1	5	11	0	0	0	E3
0	0	4	15	1	6	11	0	0	0	E2
0	0	4	6	1	7	11	0	0	0	E1
0	0	4	41	1	0	12	0	0	0	D8
0	0	4	39	1	1	12	0	0	0	D7
0	0	4	36	1	2	12	0	0	0	D6
0	0	4	33	1	3	12	0	0	0	D5
0	0	4	9	1	4	12	0	0	0	D4
0	0	4	62	1	5	12	0	0	0	D3
0	0	4	59	1	6	12	0	0	0	D2
0	0	4	50	1	7	12	0	0	0	D1

0	0	4	40	1	0	13	0	0	0	C8
0	0	4	37	1	1	13	0	0	0	C7
0	0	4	35	1	2	13	0	0	0	C6
0	0	4	34	1	3	13	0	0	0	C5
0	0	4	38	1	4	13	0	0	0	C4
0	0	4	58	1	5	13	0	0	0	C3
0	0	4	61	1	6	13	0	0	0	C2
0	0	4	57	1	7	13	0	0	0	C1
0	0	4	49	1	0	14	0	0	0	B8
0	0	4	45	1	1	14	0	0	0	B7
0	0	4	46	1	2	14	0	0	0	B6
0	0	4	43	1	3	14	0	0	0	B5
0	0	4	52	1	4	14	0	0	0	B4
0	0	4	53	1	5	14	0	0	0	B3
0	0	4	56	1	6	14	0	0	0	B2
0	0	4	63	1	7	14	0	0	0	B1
0	0	4	48	1	0	15	0	0	0	A8
0	0	4	47	1	1	15	0	0	0	A7
0	0	4	44	1	2	15	0	0	0	A6
0	0	4	42	1	3	15	0	0	0	A5
0	0	4	51	1	4	15	0	0	0	A4
0	0	4	54	1	5	15	0	0	0	A3
0	0	4	55	1	6	15	0	0	0	A2
0	0	4	60	1	7	15	0	0	0	A1
0	0	5	60	1	8	8	0	0	0	A1
0	0	5	55	1	9	8	0	0	0	A2
0	0	5	54	1	10	8	0	0	0	A3
0	0	5	51	1	11	8	0	0	0	A4
0	0	5	42	1	12	8	0	0	0	A5
0	0	5	44	1	13	8	0	0	0	A6
0	0	5	47	1	14	8	0	0	0	A7
0	0	5	48	1	15	8	0	0	0	A8
0	0	5	63	1	8	9	0	0	0	B1
0	0	5	56	1	9	9	0	0	0	B2

0	0	5	53	1	10	9	0	0	0	B3
0	0	5	52	1	11	9	0	0	0	B4
0	0	5	43	1	12	9	0	0	0	B5
0	0	5	46	1	13	9	0	0	0	B6
0	0	5	45	1	14	9	0	0	0	B7
0	0	5	49	1	15	9	0	0	0	B8
0	0	5	57	1	8	10	0	0	0	C1
0	0	5	61	1	9	10	0	0	0	C2
0	0	5	58	1	10	10	0	0	0	C3
0	0	5	38	1	11	10	0	0	0	C4
0	0	5	34	1	12	10	0	0	0	C5
0	0	5	35	1	13	10	0	0	0	C6
0	0	5	37	1	14	10	0	0	0	C7
0	0	5	40	1	15	10	0	0	0	C8
0	0	5	50	1	8	11	0	0	0	D1
0	0	5	59	1	9	11	0	0	0	D2
0	0	5	62	1	10	11	0	0	0	D3
0	0	5	9	1	11	11	0	0	0	D4
0	0	5	33	1	12	11	0	0	0	D5
0	0	5	36	1	13	11	0	0	0	D6
0	0	5	39	1	14	11	0	0	0	D7
0	0	5	41	1	15	11	0	0	0	D8
0	0	5	6	1	8	12	0	0	0	E1
0	0	5	15	1	9	12	0	0	0	E2
0	0	5	2	1	10	12	0	0	0	E3
0	0	5	11	1	11	12	0	0	0	E4
0	0	5	31	1	12	12	0	0	0	E5
0	0	5	30	1	13	12	0	0	0	E6
0	0	5	26	1	14	12	0	0	0	E7
0	0	5	24	1	15	12	0	0	0	E8
0	0	5	4	1	8	13	0	0	0	F1
0	0	5	8	1	9	13	0	0	0	F2
0	0	5	13	1	10	13	0	0	0	F3
0	0	5	27	1	11	13	0	0	0	F4
0	0	5	32	1	12	13	0	0	0	F5

0	0	5	29	1	13	13	0	0	0	F6
0	0	5	28	1	14	13	0	0	0	F7
0	0	5	25	1	15	13	0	0	0	F8
0	0	5	3	1	8	14	0	0	0	G1
0	0	5	1	1	9	14	0	0	0	G2
0	0	5	7	1	10	14	0	0	0	G3
0	0	5	12	1	11	14	0	0	0	G4
0	0	5	21	1	12	14	0	0	0	G5
0	0	5	22	1	13	14	0	0	0	G6
0	0	5	16	1	14	14	0	0	0	G7
0	0	5	19	1	15	14	0	0	0	G8
0	0	5	10	1	8	15	0	0	0	H1
0	0	5	0	1	9	15	0	0	0	H2
0	0	5	14	1	10	15	0	0	0	H3
0	0	5	5	1	11	15	0	0	0	H4
0	0	5	20	1	12	15	0	0	0	H5
0	0	5	23	1	13	15	0	0	0	H6
0	0	5	18	1	14	15	0	0	0	H7
0	0	5	17	1	15	15	0	0	0	H8

C PETsys ROOT TTree structure

The output data acquired with a PETsys TOFPET2 ASIC can be further analysed using the ROOT data analysis framework [34]. Table C.1 shows the structure of the output ROOT-file based on the TTree-class.

Table C.1: Variables of the output ROOT-file by PETsys. The variables correspond to branches of the Tree structure. Adopted from [40].

Quantity/ Variable	Data type	Unit	Comment
step1 step2	Float_t		Values of the corresponding step if thresholds are scanned
time	Long64_t	ps	Timestamp of the SiPM event using internal clock
channelID	int		Absolute channelID of the event
tot	Float_t	ns	Time-over-threshold for event. In QDC mode: time of integration. In TOT mode: difference between the time stamps of the E and t1 discriminators.
energy	Float_t	QCD: ADC units TOT: ns	Energy of the event.
tacID	string		TAC number of event, ranging from 0 to 3.
xi yi	Int_t		Pixel index position in x- and y-direction connected to channelID (see Appendix B).
x y z	Float_t		Physical coordinates of the pixel connected to channelID (see Appendix B).
tqT	Float_t	Clock period	Time for crossing the time threshold directly measured the TDC.
tqE	Float_t	Clock period	Time for crossing the energy threshold directly measured the TDC.

Bibliography

[1] Ian R. Sims and Ian W.M. Smith. Gas-phase reactions and energy transfer at very low temperatures. *Annu. Rev. Phys. Chem.*, 46(109):37, 1995.

[2] R. Atkinson. Gas-phase tropospheric chemistry of organic compounds: a review. *Atmospheric Environment*, 41:200–240, 2007.

[3] S. S. Prasad and Jr. W. T. Huntress. A model for gas phase chemistry in interstellar clouds. i - the basic model, library of chemical reactions, and chemistry among c, n, and o compounds. *The Astrophysical Journal Supplement Series*, 43:1, 1980.

[4] Mats Larsson and Ann E. Orel. *Dissociative Recombination of Molecular Ions.* Cambridge, 2008.

[5] D. R. Bates. Dissociative recombination. *Physical Review*, 78(4):492–493, may 1950.

[6] J N Bardsley. The theory of dissociative recombination. *Journal of Physics B: Atomic and Molecular Physics*, 1(3):365–380, may 1968.

[7] S. Datz et al. Branching processes in the dissociative recombination of H_3^+. *Physical Review Letters*, 74(6):896–899, 1995.

[8] O. Novotný et al. Quantum-state–selective electron recombination studies suggest enhanced abundance of primordial HeH+. *Science*, 365(6454):676–679, 2019.

[9] R. von Hahn et al. The cryogenic storage ring CSR. *Review of Scientific Instruments*, 87(6):063115, 2016.

[10] J. Öjekull et al. Dissociative recombination of NH4+ and ND4+ ions: storage ring experiments andab initiomolecular dynamics. *The Journal of Chemical Physics*, 120(16):7391–7399, apr 2004.

[11] H. Kreckel et al. High-resolution dissociative recombination of Cold H+and first evidence for nuclear spin effects. *Physical Review Letters*, 95(26), dec 2005.

[12] Arno Becker. *Imaging of Neutral Fragmentation Products from Fast Molecular Ion Beams: Paving the Way for Reaction Studies in Cryogenic Environment*. PhD thesis, Heidelberg University, 2016.

[13] Naman Jain. Electron recombination studies on titanium oxide ions in the cryogenic storage ring at the max planck institute for nuclear physics, heidelberg. Master's thesis, Indian Institute of Space Science and Technology, 2020.

[14] Steffen Novotny. Fast-beam molecular fragmentation imaging using a high-speed gated camera system. Master's thesis, Heidelberg University, 2004.

[15] Steffen Novotny. *Fragmentation of molecular ions in slow electron collisions*. PhD thesis, Heidelberg University, 2008.

[16] Proxi vision. Phosphor screens. `https://www.proxivision.de/datasheets/Phosphor-Screen-PR-0056E-03.pdf`, Version: 25.04.2021.

[17] KETEK GmbH. Sipm working principle. `https://www.ketek.net/sipm/technology/working-principle/`, Version: 23.04.2021.

[18] Stefan Gundacker and Arjan Heering. The silicon photomultiplier: fundamentals and applications of a modern solid-state photon detector. *Physics in Medicine & Biology*, 65(17):17TR01, aug 2020.

[19] SensL. Introduction to sipm – technical note. `https://www.sensl.com/downloads/ds/TN%20-%20Intro%20to%20SPM%20Tech.pdf`, 2011. Version: 16.05.2021.

[20] Martin A. Green and Mark J. Keevers. Optical properties of intrinsic silicon at 300 k. *Progress in Photovoltaics: Research and Applications*, 3(3):189–192, 1995.

[21] KETEK GmbH. Microcell construction. `https://www.ketek.net/sipm/technology/microcell-construction/`, Version: 16.05.2021.

[22] D. Renker. Geiger-mode avalanche photodiodes, history, properties and problems. *Nuclear Instruments and Methods in Physics Research Section A: Accelerators, Spectrometers, Detectors and Associated Equipment*, 567(1):48–56, 2006.

[23] M.V. Nemallapudi et al. Single photon time resolution of state of the art SiPMs. *Journal of Instrumentation*, 11(10):P10016–P10016, oct 2016.

[24] J. Riu et al. Silicon photomultiplier detector for atmospheric lidar applications. *Optics Letters*, 37(7):1229, 2012.

[25] R. Zimmermann et al. Silicon photomultipliers for improved detection of low light levels in miniature near-infrared spectroscopy instruments. *Biomedical Optics Express*, 4(5):659, 2013.

[26] S. Gundacker et al. State of the art timing in TOF-PET detectors with LuAG, GAGG and l(y)SO scintillators of various sizes coupled to FBK-SiPMs. *Journal of Instrumentation*, 11(08):P08008–P08008, aug 2016.

[27] H. S. Yoon et al. Initial results of simultaneous PET/MRI experiments with an MRI-compatible silicon photomultiplier PET scanner. *Journal of Nuclear Medicine*, 53(4):608–614, 2012.

[28] A.L. Lacaita et al. On the bremsstrahlung origin of hot-carrier-induced photons in silicon devices. *IEEE Transactions on Electron Devices*, 40(3):577–582, 1993.

[29] KETEK GmbH. Sipm device parameters. `https://www.ketek.net/sipm/technology/device-parameters/`, Version: 26.04.2021.

[30] Jean-Marie Biansan. Optgeo. `http://jeanmarie.biansan.free.fr/optgeo.html`. Version: 2.25.

[31] KETEK GmbH. Product data sheet pm3325-wb-d0. `https://www.ketek.net/wp-content/uploads/2018/12/KETEK-PM3325-WB-D0-Datasheet.pdf`, Version: 23.04.2021.

[32] PETsys Electron. SA. Petsys tofpet 2 sipm readout system - hardware user guide (v.1.6), July 2019.

[33] PETsys Electron. Petsys sipm readout system long flyer, p.4. `https://www.petsyselectronics.com/web/website/docs/products/product4/Long%20Flyer%20SiPM%20readout%20chain_v10.pdf`, Version: 10.05.2021.

[34] R. Brun et al. root-project/root: v6.22/02, 2020.

[35] Steven L. Guberman. The dissociative recombination of OH+. *The Journal of Chemical Physics*, 102(4):1699–1704, jan 1995.

[36] A. Kramida, Yu. Ralchenko, J. Reader, and and NIST ASD Team. NIST Atomic Spectra Database (ver. 5.8), [Online]. Available: `https://physics.nist.gov/asd`

[2021, June 5]. National Institute of Standards and Technology, Gaithersburg, MD., 2020.

[37] U. Hechtfischer et al. Near-threshold photodissociation of cool OH+to o $^+$ h+ and o+ + h. *The Journal of Chemical Physics*, 151(4):044303, jul 2019.

[38] KETEK GmbH. private communication, 18.03.2021.

[39] O. Novotný et al. Dissociative recombination measurements of chloronium ions (d2cl+) using an ion storage ring. *The Astrophysical Journal*, 862(2):166, aug 2018.

[40] PETsys Electron. SA. Petsys tofpet 2 sipm readout system - software user guide (v.2019.09), September 2019.

Erklärung

Ich versichere, dass ich diese Arbeit selbstständig verfasst habe und keine anderen als die angegebenen Quellen und Hilfsmittel benutzt habe.

Heidelberg, den 10.06.2021 ....